remote sensing

MDPI

Article

Integrating EO/GIS Suitability and Flood Dynamics for Nature-Based Solutions Siting: A Flood Digital Twin Application

Aristotelis-Ilias Ganos, Ierotheos Zacharias, Athanasios Chassiakos * and Olympia Ageli

Department of Civil Engineering, University of Patras, 26504 Patras, Greece; ganos.a@ac.upatras.gr (A.-I.G.); izachari@upatras.gr (I.Z.); civ7235@ac.upatras.gr (O.A.)
* Correspondence: a.chassiakos@upatras.gr

Highlights

What are the main findings?

- All portfolios reduced flood impacts; hydrodynamically informed NbS siting added only 1.5–2.6 percentage points to building-exposure reductions and did not consistently reduce inundation area.
- Mechanism-specific siting showed no consistent advantage; strategy rankings depended on rainfall intensity, performance metric, and evaluation mask.

What are the implications of the main findings?

- Hydrodynamic information mainly changed where NbS were placed; its effect on overall performance was small and objective-dependent.
- NbS portfolios require multi-event, multi-metric evaluation, including checks for local adverse effects.

Abstract

The flood-mitigation effect of Nature-Based Solutions (NbS) depends both on site suitability and on their position within catchment-scale flood processes. Earth Observation (EO) and GIS methods support spatial planning, but the added value of different forms of flood-dynamics information for NbS siting remains unclear. This study develops a framework that combines EO/GIS-based candidate generation, general and intervention-specific siting indicators derived from a single baseline simulation, resource-constrained portfolio optimisation, and hydraulic performance evaluation. Applied to the Mandra catchment, Greece, the framework generated 1446 candidates across four NbS types. Three siting strategies (static suitability and suitability combined with general or mechanism-specific hydrodynamic indicators) were compared under 40 mm/h design and 70 mm/h stress-test events of 60 min. All portfolios reduced inundated area exceeding 0.10 m by 8.81–9.57% (design) and 4.11–4.63% (stress-test), and buildings exposed above 0.30 m by 19.48–22.07% and 7.10–9.39%. Differences between strategies were small: hydrodynamically informed siting reduced building exposure by a further 1.5–2.6 percentage points, but not consistently in inundated areas, and mechanism-specific indicators did not consistently outperform general ones. Integrated into a Flood Digital Twin, the precomputed outcomes support the examination of planning trade-offs.

Keywords: Nature-Based Solutions; Earth Observation; Sentinel-2; flood mitigation; GIS-based suitability; hydrodynamic modelling; spatial prioritisation; resource-constrained optimisation; Flood Digital Twin

Check for updates

Academic Editors: Bo Chen, Yao Li, Wanji Zheng and Chuang Song

Received: 30 October 2026
Revised: 20 November 2026
Accepted: 24 November 2026
Published: 28 November 2026

Copyright: © 2026 by the authors. Licensee MDPI, Basel, Switzerland. This article is an open access article distributed under the terms and conditions of the Creative Commons Attribution (CC BY) license.

1. Introduction

Flood-risk management extends beyond forecasting and emergency response to include preventive interventions that modify how surface runoff is generated, concentrated, and conveyed towards exposed areas. Nature-Based Solutions (NbS) have emerged as a complementary approach to conventional flood-protection infrastructure, promoting natural processes that enhance infiltration, attenuate surface flow, and provide temporary water storage [1,2]. These functions can be supported through interventions ranging from vegetation and soil restoration to riparian buffers, small flow-retention structures, and detention areas. Their effectiveness depends on intervention characteristics, catchment conditions, spatial placement, and the magnitude of the rainfall event.

Consequently, NbS planning is a spatial problem. A location that is physically suitable for a particular intervention is not necessarily the location where that intervention can provide the greatest flood-mitigation benefit. Different parts of a catchment contribute to flooding through distinct processes: some generate substantial surface runoff, others concentrate and convey flow, while others offer opportunities for temporary retention before floodwaters reach downstream settlements. Effective planning must therefore consider both the spatial suitability of an intervention and the hydrological or hydrodynamic significance of its location.

Earth Observation (EO) data, Geographic Information Systems (GIS), and multi-criteria decision analysis provide a basis for identifying spatial opportunities and constraints for NbS implementation. Such approaches combine terrain characteristics, land cover, vegetation conditions, drainage proximity, and available space to assess the suitability of alternative locations. Kuller et al. [3] developed a planning-support tool for green stormwater infrastructure based on spatial suitability, while Asare et al. [4] applied spatial multi-criteria analysis to identify locations suitable for different flood-mitigation NbS in Accra, Ghana. However, physical suitability does not directly establish how modifying a particular location will alter flood propagation or downstream exposure.

Previous research has addressed this distinction by incorporating hydrological connectivity, flood-source areas, flow pathways, and exposed receptors into spatial planning. Vercruysse et al. [5] developed source-to-impact criteria for identifying priorities in urban flood management, while Dawson et al. [6] examined spatial opportunities for integrated flood-management infrastructure. Iliadis et al. [7] linked runoff-contributing areas with exposed buildings through a source–receptor framework, and Parretta et al. [8] combined spatial suitability with hydrological and hydraulic indicators for NbS prioritisation. Reinstaller et al. [9] further assessed blue–green infrastructure placement using flood-hazard and urban-heat priority maps, comparing modelled benefits at higher- and lower-priority locations.

A second line of research represents and evaluates NbS portfolios using hydrological or hydrodynamic models, often in combination with optimisation methods. Ur Rehman et al. [10] coupled multi-objective optimisation with a detailed flood model to determine blue–green infrastructure locations, while Azadgar et al. [11] combined a genetic algorithm with the InVEST Urban Flood Risk Mitigation model to optimise NbS placement against retention and cost objectives. In a regional application in Western Attica, Theochari and Baltas [12] evaluated land-cover changes and retention ponds under alternative climate scenarios using hydrological modelling. Sedighkia et al. [13] recommended matching hydrological and hydrodynamic modelling approaches to intervention mechanisms and spatial scales, and a recent review describes Flood Digital Twins as environments for scenario exploration and flood-risk decision support [14]. Intervention performance in model-based assessments is also sensitive to rainfall characteristics, and spatial configurations that

perform favourably under one event may not retain the same relative effectiveness under more severe conditions [10,15].

These studies differ in their candidate-generation procedures, selection constraints, and evaluation objectives. As a result, it remains unclear how the representation of flood dynamics within the siting process affects the performance of the selected portfolios. Isolating this effect requires a directly comparable assessment with explicitly defined siting strategies, a shared initial candidate space, comparable intervention resources, and consistent hydrodynamic performance evaluation.

The objective of this study is to develop and evaluate an integrated framework for preliminary NbS planning that combines EO/GIS-based spatial suitability, simulated flood dynamics, resource-constrained portfolio selection, and hydrodynamic performance assessment. The framework is applied to the Mandra catchment, Greece, considering four intervention types associated with runoff generation reduction, flow-path attenuation, and temporary water storage. Three siting strategies are compared: static EO/GIS suitability (C1), suitability combined with general hydrodynamic importance (C2), and suitability combined with mechanism-specific hydrodynamic relevance (C3). The strategies share a common initial candidate space and comparable intervention-resource targets, although C3 additionally excludes candidates with structurally zero mechanism-specific relevance. The selected portfolios are evaluated under a design rainfall event and a more severe stress-test event, without redesigning the interventions. The principal methodological contribution is the structured comparison of these alternative siting strategies under consistent evaluation conditions, while integration into a Flood Digital Twin supports the spatial examination of their precomputed outcomes.

The investigation addresses three research questions: (i) To what extent does adding simulated flood-dynamics information to EO/GIS suitability influence intervention selection and flood-mitigation performance? (ii) Does matching hydrodynamic indicators to the functional mechanisms of individual NbS types provide additional benefits over general hydrodynamic prioritisation? (iii) Do the beneficial effects and relative performance of the selected portfolios persist under increased rainfall intensity and changes in rainfall temporal distribution?

2. Materials and Methods

The proposed methodology establishes a three-stage computational workflow integrating EO, geospatial analysis, and hydrodynamic modelling for the spatial planning and performance assessment of NbS (Figure 1). The workflow is presented through its implementation in the Mandra catchment, while the specific datasets, parameter values, and spatial thresholds adopted in this application are not intended as universal requirements of the methodology. The hydrodynamic modelling component builds on the previously published approach of Ganos et al. [16]. The methodological development of the present study focuses on NbS candidate generation, static and hydrodynamic siting indicators, resource-constrained portfolio selection, and comparative evaluation of intervention configurations.

The first stage establishes a consistent geospatial and hydrodynamic information base. EO and complementary GIS datasets are processed to characterise terrain, land cover, vegetation, drainage characteristics, and spatial constraints relevant to NbS planning. In parallel, a baseline hydrodynamic simulation characterises flood conditions without the proposed interventions. The resulting spatial layers and simulated flood-dynamics indicators provide the information required for candidate generation, suitability assessment, and hydrodynamically informed prioritisation.

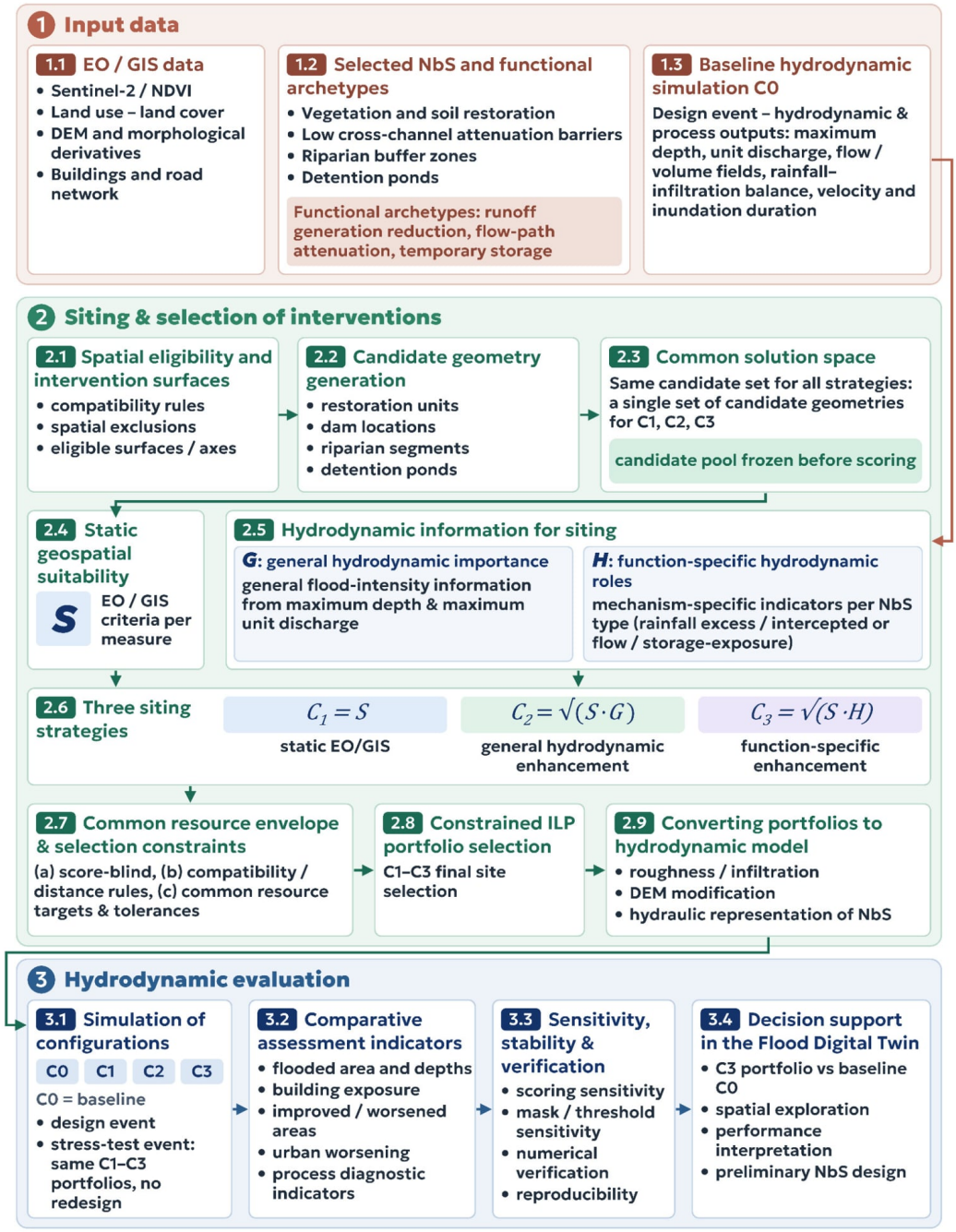

Figure 1. Overall methodological workflow for EO/GIS- and flood-dynamics-informed NbS planning and hydrodynamic evaluation.

The second stage generates and selects intervention portfolios. Spatial eligibility and geometric rules are first applied to establish a common pool of candidate interventions independently of simulated flood conditions. Candidates are then scored under the three siting strategies: static geospatial suitability (C1), suitability combined with general hydrodynamic information (C2), and suitability combined with mechanism-specific hydrodynamic information (C3). Resource-constrained optimisation produces alternative portfolios under predefined intervention targets and spatial compatibility constraints, which are then translated into hydrodynamic model inputs.

The third stage evaluates the selected portfolios through comparative hydrodynamic simulations. Each intervention configuration is assessed against the corresponding baseline under the design and stress-test rainfall events, without modifying the selected interven-

tions between events. Flood-performance indicators, spatial comparisons, and sensitivity analyses are used to examine mitigation benefits, differences between strategies, and potential local adverse effects. The resulting portfolios and precomputed simulation outcomes are integrated into the Flood Digital Twin to support the spatial exploration and comparison of alternative planning decisions.

2.1. Geospatial and Hydrodynamic Information Base

2.1.1. Study Area and Geospatial Datasets

The study was conducted in the Mandra catchment, in Western Attica, Greece. On 15 November 2017, a flash flood in the town of Mandra caused 24 fatalities and extensive damage to property and infrastructure [17,18]. The catchment was selected because of this event and because surface runoff generated in its upstream parts is collected and rapidly conveyed towards the downstream urban area. NbS performance can therefore be examined under the large runoff volumes that accumulate before the flow enters the town. The 10 m DEM comprises 609,439 valid (non-NoData) cells, corresponding to approximately 60.9 km^2. Following the application of the model boundary conditions, 609,395 cells remain as active (core) computational nodes (Section 2.3.2). A common geospatial framework was established to support the identification of feasible NbS locations, the generation of candidate intervention geometries, and their subsequent hydrodynamic evaluation.

EO data were primarily obtained from the Copernicus Sentinel-2 mission and the Copernicus Land Monitoring Service (CLMS). Four precomputed quarterly Sentinel-2 composites for 2025 were used to calculate the Normalised Difference Vegetation Index (NDVI) from the near-infrared (B08) and red (B04) spectral bands, both available at 10 m resolution. The pixel-wise median of the four NDVI observations was adopted as a representative indicator of vegetation condition and used in the suitability assessment of vegetation and soil restoration measures and riparian buffers. The Level-3 quarterly mosaics were generated from cloud-masked Sentinel-2 Level-2A observations using the provider's compositing procedure; no additional scene-level cloud-cover filtering was applied in this study.

Land-cover information was obtained from CORINE Land Cover 2018, comprising 13 classes within the study area. These classes provided the principal thematic basis for determining land-use compatibility and spatial eligibility for different NbS types. The CORINE land-cover classes were aligned with the common 10 m grid for spatial analysis, while retaining the thematic detail and limitations of the original dataset. Geological data were obtained from the online geospatial services of the Hellenic Survey of Geology and Mineral Exploration (HSGME/EAGME) through its official geoportal [19], accessed in February 2026. The retrieved geological information was incorporated into the GIS-based suitability assessment. Figure 2 presents the study area and the principal EO-derived spatial layers.

The original SRTM elevation data (acquired in February 2000 and retrieved in February 2026), with an approximate native spatial resolution of 30 m, were hydrologically conditioned and resampled to establish a common 10 m computational grid, following the preprocessing approach described by Ganos et al. [16]. The finer grid spacing was adopted to align the terrain with building locations and other geospatial layers, rather than to increase the underlying topographic information. Consequently, terrain features and flow pathways smaller than the effective resolution of the source elevation data may not be adequately represented. Terrain slope and the Topographic Position Index (TPI) were derived from the Digital Elevation Model (DEM), together with hydrological descriptors including D8 flow direction, flow accumulation, drainage-network geometry, distance to the drainage network, and subcatchment boundaries. These datasets supported intervention eligibility, candidate generation, and static-suitability assessment. The TPI was calculated

in QGIS (v3.30.2) using the GDAL implementation (default 15 × 15-cell moving window, i.e., 150 × 150 m). Flow accumulation and drainage directions were derived using GRASS GIS (v 2.12.99) r.watershed, with a minimum exterior watershed basin size of 500 cells. The drainage network was subsequently extracted using r.stream.extract, with a minimum contributing-area threshold of 5000 cells (0.5 km^2 at 10 m resolution).

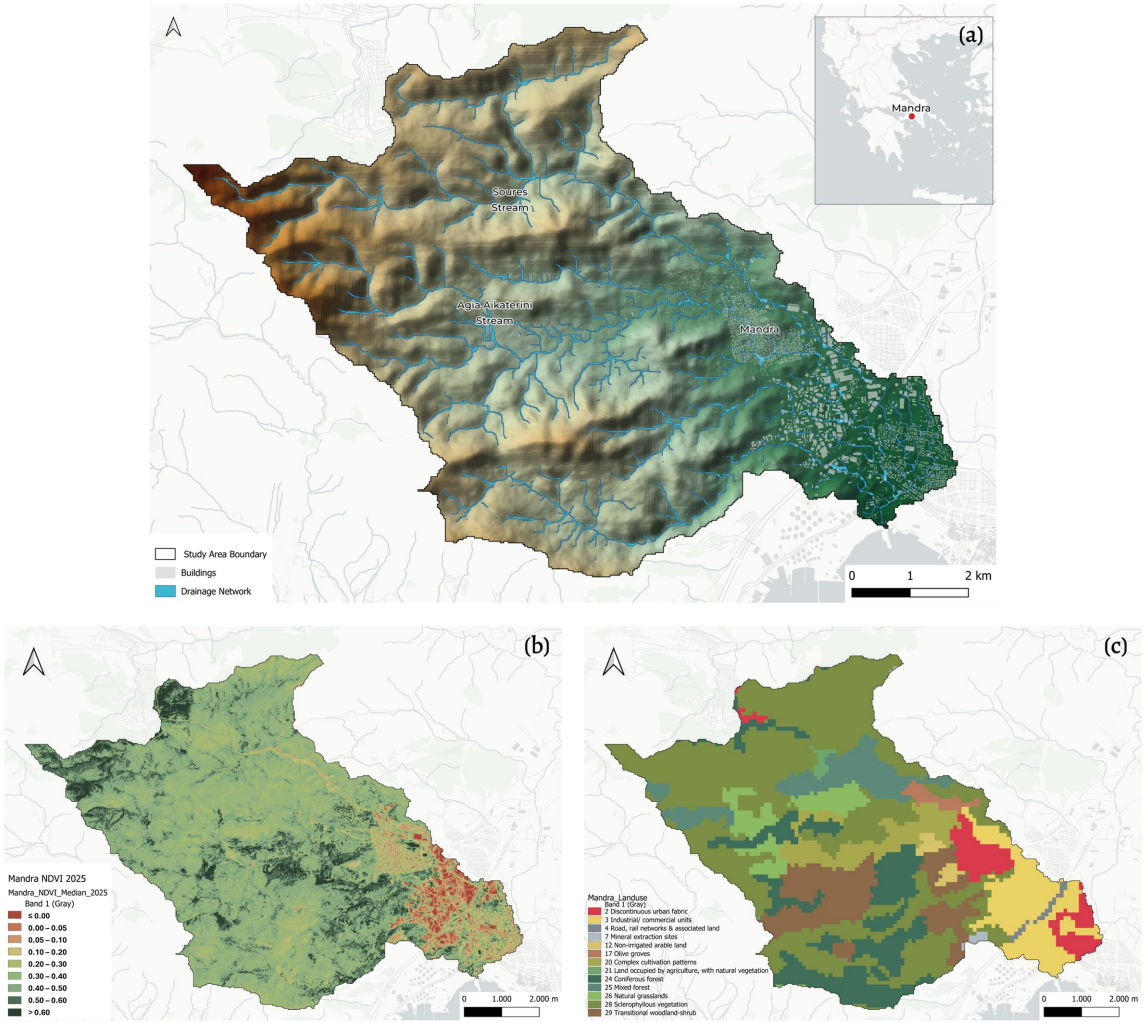

Figure 2. Study area and geospatial datasets: (**a**) Mandra catchment and topography; (**b**) median NDVI (2025); and (**c**) CORINE Land Cover (2018).

Building footprints (n = 6753) and road network (approximately 239 km) were obtained from Microsoft's Bing Maps open geospatial datasets (Global ML Building Footprints and Road Detections, respectively), accessed in February 2026. Their underlying imagery may have different acquisition dates. Corresponding raster representations were aligned with the common 10 m grid to support spatial exclusion rules and flood-exposure assessment.

The datasets were assigned distinct methodological roles rather than being uniformly incorporated into a single suitability index. Depending on their characteristics, they were used as eligibility constraints, suitability criteria, geometric inputs, or complementary diagnostic information (Table 1). The hydrodynamic information required for candidate prioritisation was derived separately from the baseline simulation described in the following section.

Table 1. Principal EO and geospatial datasets used in the NbS planning framework, with their temporal or spatial characteristics and methodological roles.

Dataset	Source and Characteristics	Methodological Role
Sentinel-2 MSI	Quarterly composites, 2025; B04 and B08 at 10 m	Median NDVI; vegetation-related suitability
CORINE Land Cover	CLMS, 2018; 13 classes	Land-use compatibility & eligibility
DEM & terrain derivatives	SRTM (initially 30 m) → hydrologically corrected DEM in 10 m; slope & TPI	Common grid, geomorphology, suitability & candidate generation
Hydrological derivatives	D8 flow direction, flow accumulation, drainage network, stream proximity & subcatchments	Hydrological connectivity & spatial constraints
Buildings & road network	6753 buildings & 239 km of roads	Spatial exclusions & building-exposure assessment

2.1.2. Baseline Hydrodynamic Simulation

The baseline hydrodynamic response of the Mandra catchment was represented by configuration C0, corresponding to the existing terrain and surface conditions without the proposed NbS interventions. The simulation employed Landlab OverlandFlow (v2.8.0) [20], building on the modelling approach developed and evaluated by Ganos et al. [16]. Whereas the previous study coupled 10 m catchment and 2 m urban grids, the present analysis used a single, hydrologically conditioned 10 m computational grid aligned with the geospatial layers used for NbS planning.

To assess the flood-extent representation of the single-grid 10 m hydrodynamic model, a retrospective comparison was performed against the observed inundation footprint of the November 2017 Mandra event, reconstructed from drone imagery and interpolated high-water marks by Andreadakis et al. [21] and digitised for this study. The comparison was restricted to approximately 2.91 km^2 urban area covered by the reference dataset. A separate simulation was conducted using spatially and temporally uniform rainfall of 25 mm/h for 6 h (150 mm in total). This simplified rainfall forcing was intended to approximate the event's accumulated rainfall. At a maximum-depth threshold of 0.10 m, the model reproduced 77.8% of the observed inundated area within the common comparison domain, with a critical success index (CSI) of 0.606. The simulated extent exceeded the observed footprint in some locations, with 26.8% of the simulated inundated area falling outside the observed extent. These results provide evidence of spatial flood-extent agreement for the single-grid configuration, although they do not establish the accuracy of local inundation depths or building-level exposure estimates.

The baseline design-event simulation provided the hydrodynamic information required for candidate scoring, while C0 served as the reference configuration for evaluating the selected portfolios under each rainfall event. Infiltration was accounted for through the hydrological routines of the existing modelling framework [16]. The numerical settings were kept consistent across the baseline and intervention configurations, except for the prescribed changes in terrain elevation, surface roughness, and infiltration-related parameters associated with the selected NbS. The baseline design event (I040_D060) consisted of spatially and temporally uniform rainfall at 40 mm/h for 60 min. The selected intensity represents a rounded approximation of the 50-year, 60 min areal design rainfall intensity (37.11 mm/h), as derived from the applicable intensity–duration–frequency (IDF) relationships [22]. The IDF estimates were obtained from the updated nationwide rainfall-frequency parameters, using area-weighted contributions from the ten 5 × 5 km grid cells intersecting the Mandra

catchment (60.95 km^2) and applying the areal reduction relationship of Koutsoyiannis and Xanthopoulos [23]. The corresponding estimated 1000-year, 60 min areal rainfall intensity was 72.1 mm/h. Accordingly, a rounded intensity of 70 mm/h was adopted for the extreme stress-test event (I070_D060) to examine the performance of the unchanged NbS portfolios under substantially increased rainfall forcing, without implying that the scenario represents an exact 1000-year event. The total simulation period was 3 h, comprising 60 min of rainfall followed by 120 min to capture the subsequent flood evolution and recession.

The OverlandFlow component is based on the de Almeida [24] local-inertial approximation of the two-dimensional shallow-water equations. The simulations employed a momentum weighting factor of $\theta = 1$, corresponding to the Bates-type formulation [25], and adaptive time stepping with $\alpha = 0.9$. The steep-slope option was enabled, limiting link discharge to a Froude number of 1. The model was initialised with a uniform water film of 1.01 mm and zero discharge. External grid boundaries and NoData cells were closed, while downstream drainage was represented by a fixed-value outlet node and adjacent coastal sink cells, where water depth was reset after each time step. Flow-related quantities were retained at their computational-grid links for subsequent association with candidate intervention geometries, while the maximum-depth field was used to characterise building exposure and identify downstream receptors. Representative baseline fields are shown in Figure 3.

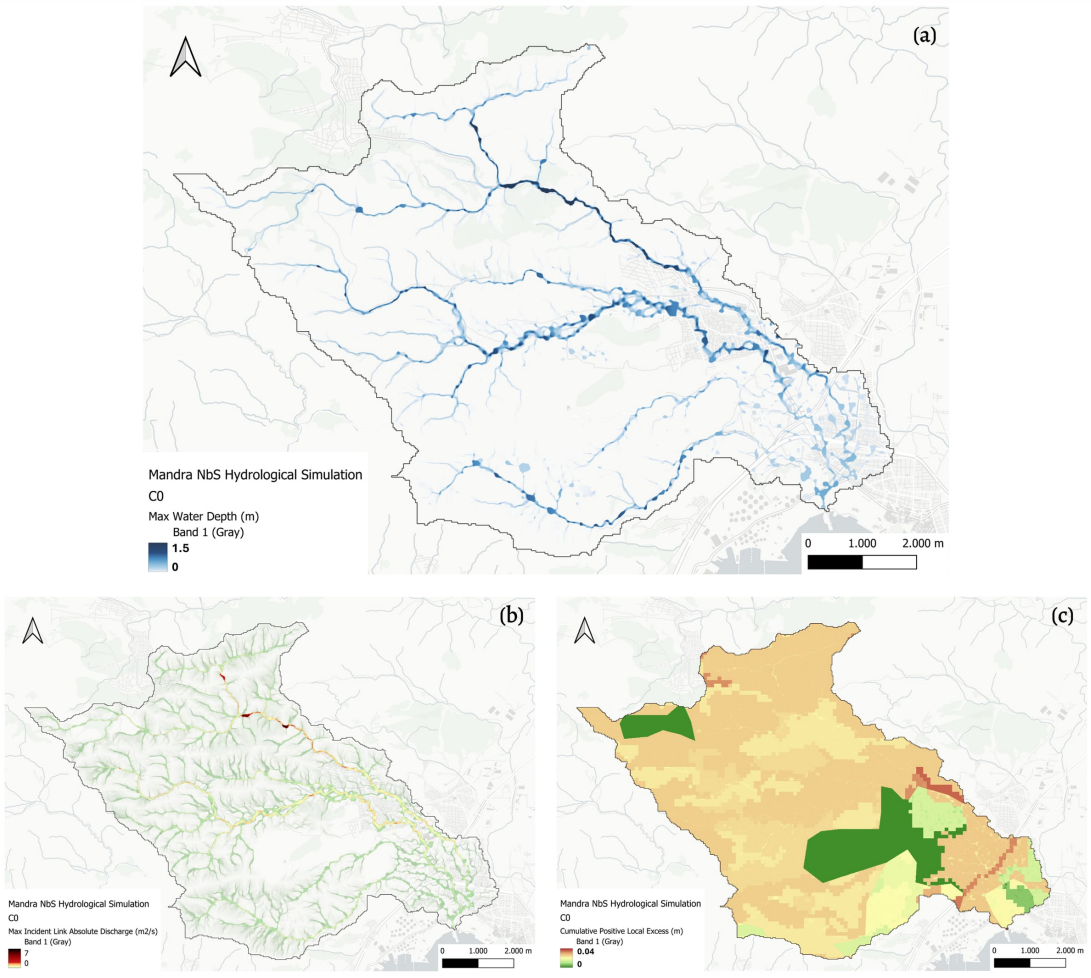

Figure 3. Baseline hydrodynamic fields (C0): (**a**) maximum water depth; (**b**) maximum unit discharge; and (**c**) cumulative positive rainfall–infiltration excess.

Surface roughness was assigned according to CORINE land-cover classes, with Manning's coefficients ranging from 0.02 to 0.18. Infiltration was represented using the Green–Ampt (Mein-Larson) formulation [26], with hydraulic properties derived from geological units and saturated conductivity adjusted by a land-cover-dependent pervious fraction. For the scree geological unit, the saturated conductivity was set to 1×10^{-5} m/s. Infiltration was limited by the available surface water, without imposing a maximum soil-storage capacity. Evapotranspiration was not included in these simulations.

Several spatially distributed indicators were extracted from the baseline simulation to characterise the hydrodynamic behaviour of the catchment. These included maximum water depth, maximum unit discharge, maximum flow velocity, inundation duration, cumulative infiltration, and time-integrated flow quantities. Particular attention was given to the local positive rainfall–infiltration excess, calculated by accumulating the positive difference between rainfall and infiltration at each computational cell. Unlike cumulative infiltration, which may also account for water originating from upstream areas, this indicator provides information on the local tendency for surface runoff generation.

2.2. NbS Candidate Generation and Portfolio Design

2.2.1. NbS Typologies and Candidate Generation

Four NbS intervention types were selected for the Mandra application to represent three complementary flood-mitigation mechanisms that could be implemented within the existing hydrodynamic modelling framework: runoff generation reduction, flow-path attenuation, and temporary water storage. Vegetation and soil restoration targets runoff generation by increasing surface roughness and infiltration capacity. Low cross-channel check dams and riparian buffers address concentrated flow propagation through local retention and increased hydraulic resistance, respectively. Detention ponds provide temporary storage of floodwater before its downstream conveyance. Check dams and detention ponds are treated as hybrid measures, as their classification as nature-based depends on site-specific design (Section 4.5). The selected intervention types were intended to provide a representative range of hydraulic functions for comparing alternative siting strategies, rather than an exhaustive assessment of NbS options applicable to the catchment.

Spatial eligibility was assessed separately for each intervention type using land-cover compatibility, terrain characteristics, drainage-network geometry, and built-environment constraints. Thirteen CORINE Land Cover classes were classified as permitted, conditionally eligible, or excluded for each measure. Buildings, roads, and incompatible land uses were excluded, while measure-specific terrain and hydrological constraints further restricted the available intervention areas. Conditionally eligible locations were retained for spatial assessment but were not automatically admitted to final portfolio selection. The resulting eligible intervention domains comprised approximately 3922.8 ha for restoration, 42.3 km of stream network for check dams, 233.4 ha for riparian buffers, and 911 ha for detention ponds.

Within these domains, candidate interventions were generated as discrete spatial geometries using predefined, measure-specific rules. Restoration units were derived from a regular 200 m grid clipped to eligible land. Candidate check dams were generated at 100 m intervals along eligible channel reaches, with cross-sections constructed perpendicular to the local flow direction and screened against geometric and infrastructure constraints. Riparian candidates were delineated along 200 m channel segments, considering 20 m buffer zones independently on each bank. Detention-pond candidates were developed from local topographic depressions, subject to predefined limits on slope, area, storage capacity, excavation volume, and geometry. The sampling intervals, geometric criteria, and screening thresholds, together with the resulting candidate counts, are summarised in Table 2.

Table 2. NbS intervention types, candidate-generation criteria, and resulting candidate counts.

NbS Intervention	Functional Mechanism	Principal Generation Criteria	Candidates
Vegetation and soil restoration	Runoff reduction	200 m grid; ≥60% eligible area; ≥1 ha	958
Check dams	Flow-path attenuation	100 m sampling interval; crest length 20–160 m	282
Riparian buffers	Flow-path attenuation	200 m channel segments; 20 m per bank	187
Detention ponds	Temporary storage	Slope ≤ 5°; area 0.5–8 ha; storage ≥ 2000 m^3	19

In total, 1446 candidate interventions were generated from static geospatial information (Table 2; Figure 4).

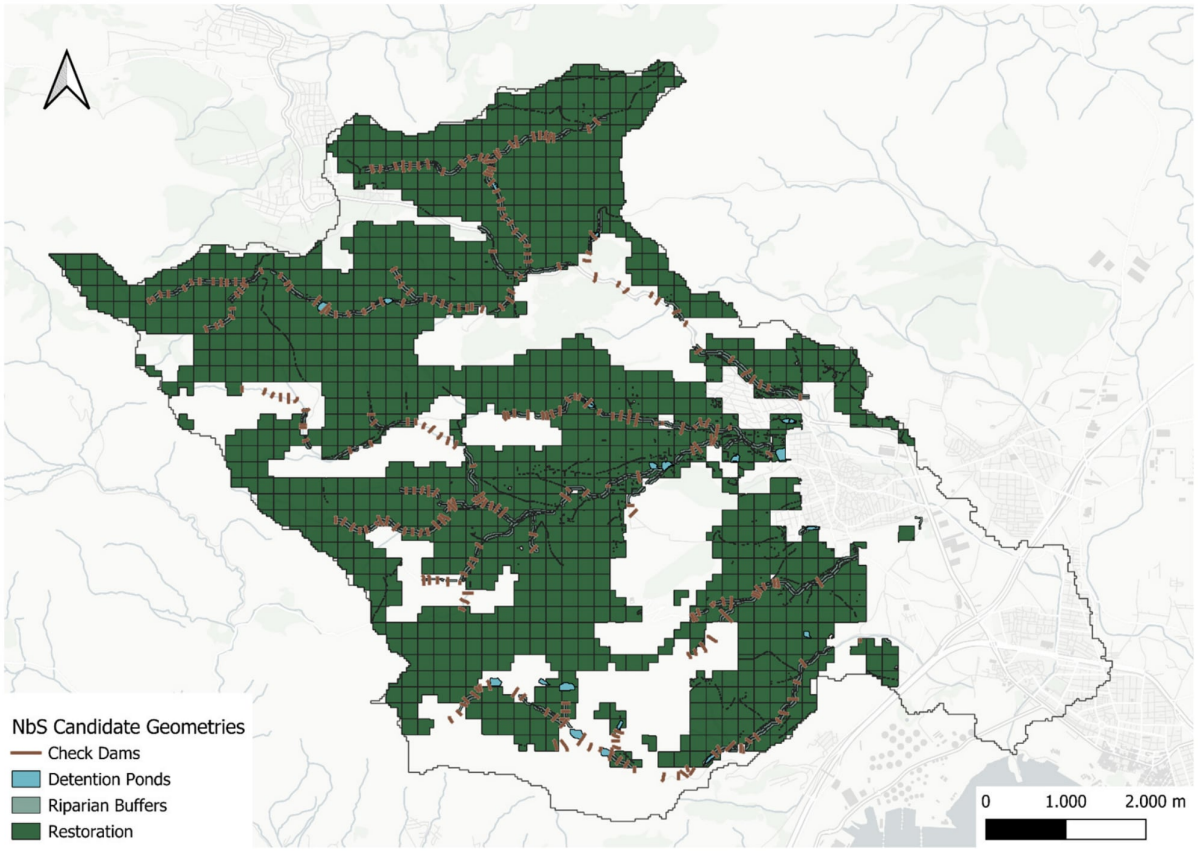

Figure 4. Spatial distribution of the generated NbS candidate interventions across the Mandra catchment.

The candidate geometries were established independently of simulated flood conditions and retained as the common initial candidate pool for C1–C3. Candidate scoring used geospatial attributes and hydrodynamic indicators extracted from the shared C0 design-event simulation; no separate hydrodynamic simulation was performed for each candidate. Full simulations were conducted only for the baseline and the selected intervention portfolios under the two rainfall events, resulting in eight core simulations (Section 2.3.1).

2.2.2. Suitability and Flood-Dynamics Scoring

Following candidate generation, three composite siting indicators were calculated: static geospatial suitability (S), general hydrodynamic importance (G), and mechanism-specific hydrodynamic relevance (H). The indicators serve distinct purposes: S characterises physical suitability using EO/GIS information, whereas G and H incorporate different aspects of the simulated baseline flood response. All three were evaluated separately within each NbS type and used to prioritise candidate locations. They should be distinguished from the final flood-performance indicators, which were calculated after hydrodynamic simulation of the selected portfolios.

Static Geospatial Suitability (S):

Static suitability was assessed using measure-specific criteria derived from EO, terrain, hydrological, and geometric information, without incorporating simulated flood conditions. These criteria reflected the physical characteristics relevant to each intervention, including vegetation condition, slope, upstream contributing area, spatial continuity, and available storage capacity (Table 3).

Table 3. Static-suitability criteria and mechanism-specific hydrodynamic indicators for each NbS type.

NbS Type	Static-Suitability Criteria (S) *	Mechanism-Specific Hydrodynamic Information (H)
Vegetation and soil restoration	NDVI ↓, slope ↓, spatial coherence ↑	Mean positive local rainfall–infiltration excess
Check dams	Crest length ↓, contributing area ↑, channel slope ↓, continuity ↑, building distance ↑	Total flow volume and summed link-wise peak flows across the candidate crest
Riparian buffers	Available area ↑, continuity ↑, NDVI ↓, slope ↓	Median throughflow volume and maximum local peak-flow indicator
Detention ponds	Storage capacity ↑, TPI ↓, slope ↓, drainage distance ↓, contributing area ↑, compactness ↑	Absolute integrated flow volume and potentially exposed building count along associated/downstream network reaches

* NDVI: Normalised Difference Vegetation Index; TPI: Topographic Position Index; spatial coherence: equally weighted combination of the eligible-area fraction and the Polsby–Popper compactness of the largest eligible component within each restoration unit; continuity: uninterrupted eligible channel length for check dams and the available fraction of the 20 m bank strip for riparian buffer; compactness: calculated as $4\pi A/P^2$, where A and P denote polygon area and perimeter, respectively. These indicators are used in candidate eligibility screening and suitability scoring, rather than as portfolio-level spatial constraints. Upward (↑) and downward (↓) arrows indicate whether higher or lower criterion values, respectively, are preferred in the static-suitability ranking. All criterion rankings are calculated separately within each NbS type. General hydrodynamic importance (G) is defined in Equation (2).

To combine variables expressed in different units, a rank-based normalisation procedure was applied. For each NbS type, candidate interventions were independently ranked according to each criterion, considering its predefined favourable direction. Rankings were normalised to the interval $[0, 1]$, with higher values indicating more favourable conditions. Tied observations received average ranks.

For candidate i of intervention type m, the initial suitability score was calculated as:

$$S_{i,m}^{raw} = \frac{1}{K_m} \sum_{j=1}^{K_m} r_{i,j} \quad (1)$$

where K_m denotes the number of active criteria for intervention type m, and $r_{i,j}$ is the normalised rank of candidate i for criterion j. The resulting scores were ranked again within

each intervention type to obtain the final suitability indicator S. This secondary normalisation ensured a consistent relative scale for subsequent combination with hydrodynamic indicators. Strongly redundant criteria were excluded from the final scoring scheme, while candidates with missing values in any active criterion were not considered for final selection.

General Hydrodynamic Importance (G):

The general hydrodynamic indicator G was introduced to identify candidate locations exhibiting high flood activity, independently of the functional mechanism of the proposed intervention. It was derived from two complementary outputs of the baseline C0 simulation: maximum water depth, representing local water accumulation, and maximum unit discharge, representing flow conveyance intensity. For each intervention type, the corresponding hydrodynamic quantities were converted into normalised relative ranks and combined with equal weighting:

$$G_i^{raw} = \frac{r_{h,i} + r_{q,i}}{2} \quad (2)$$

where $r_{h,i}$ and $r_{q,i}$ represent the normalised ranks associated with maximum water depth and maximum unit discharge, respectively. The indicator therefore favoured locations characterised by both substantial inundation depth and intense flow conveyance. Maximum velocity was retained as a diagnostic variable but excluded from G to avoid introducing additional correlated information. Similarly, products of independently determined maximum depth and velocity were not employed, since these maxima do not necessarily occur simultaneously.

Mechanism-Specific Hydrodynamic Relevance (H):

While G provides a general characterisation of flood activity, it does not distinguish between locations where runoff is generated, conveyed, or potentially retained. To address this limitation, a mechanism-specific indicator H was developed by matching hydrodynamic information to the intended function of each NbS type.

For vegetation and soil restoration, H was based on the mean cumulative positive rainfall–infiltration excess within each candidate area, which represents the local tendency for runoff generation, rather than water conveyed from upstream locations (Section 2.1.2). The corresponding values were ranked within the restoration candidate set.

For all flow-based components of H, time-integrated flow volumes were calculated from the absolute unit discharge at each computational link, integrated over the full 10,800 s simulation period and multiplied by the 10 m link width. Absolute values were accumulated at each time step, so flow reversals contributed positively. Signed cumulative discharge was retained separately for water-balance diagnostics and was not used in candidate scoring.

For check dams, hydrodynamic relevance was evaluated using the time-integrated flow volume and the sum of link-wise peak flows across the candidate crest. The two quantities were ranked independently and combined using their geometric mean, representing the relative importance of flow interception at each location.

For riparian buffers, the corresponding indicator characterised flow conveyance along the associated channel segment. The median time-integrated throughflow volume and maximum flow-intensity indicator were obtained from adjacent computational links and combined through the geometric mean of their normalised ranks. This spatial aggregation avoided repeatedly counting the same flow along successive channel cells.

For detention ponds, H combined the time-integrated flow volume at a nearby drainage-network cell with a proxy for potentially exposed buildings along the associated drainage network. Each pond candidate was associated with the highest-flow network cell within 150 m of its boundary. Buildings with baseline design-event maximum depths exceeding 0.10 m at their centroids were assigned to the nearest drainage-network reach within

300 m. The building indicator counted those assigned to the pond-associated reach and all downstream reaches, following the directed network topology. Consequently, buildings could be associated with multiple pond candidates, while buildings on the same reach were not necessarily located strictly downstream of the pond. The two indicators were combined using the geometric mean of their normalised ranks.

All mechanism-specific quantities were evaluated using the same baseline C0 design event and expressed as relative rankings within their respective intervention types. A structurally zero hydrodynamic role ($H = 0$) was assigned when the baseline simulation provided no meaningful evidence of the intervention's intended function.

For vegetation and soil restoration, $H = 0$ was assigned when the candidate-mean cumulative positive rainfall–infiltration excess, after subtracting the rainfall depth of the first computational time step, did not exceed an absolute numerical tolerance of 1×10^{-5} m (0.01 mm). This correction accounts for the initial model step, during which rainfall is applied before infiltration becomes active. In the baseline design-event simulation, the initial step lasted 90.44 s, contributing 1.005 mm of rainfall. The resulting classification identified 79 of 958 restoration candidates with $H = 0$. Their corrected excess values did not exceed 0.0037 mm, whereas all remaining candidates exceeded 0.0487 mm. The classification was unchanged when the numerical tolerance was varied between 0.004 and 0.048 mm. A separate post-processing consistency test confirmed that adjusting the first-step rainfall contribution simultaneously in the cumulative excess and its threshold did not change the classification.

For detention ponds, a zero role was assigned when either the associated flow-volume proxy or the potentially exposed building count was zero. These zero values were preserved during rank normalisation. The three indicators provided the basis for the alternative siting strategies introduced in Section 2.2.3.

2.2.3. Siting Strategies and Portfolio Optimisation

Alternative Siting Strategies:

Three alternative siting strategies were developed to examine the contribution of different levels of hydrodynamic information to NbS planning. All strategies originated from the same predefined candidate pool and employed the siting indicators described in Section 2.2.2. Before their combination, the composite indicators S, G, and H were re-ranked within each NbS type to ensure a common relative scale. Tied values received average ranks, while structurally zero hydrodynamic roles were preserved. The candidate score under each strategy was defined as:

$$Score_i^{C1} = S_i \tag{3}$$

$$Score_i^{C2} = \sqrt{S_i G_i} \tag{4}$$

$$Score_i^{C3} = \sqrt{S_i H_i} \tag{5}$$

Strategy C1 represents conventional geospatial suitability-based planning, relying exclusively on static EO/GIS-derived information. Strategy C2 combines geospatial suitability with general hydrodynamic importance, favouring locations exhibiting both suitable physical characteristics and intense flood activity. Strategy C3 replaces general hydrodynamic importance with the mechanism-specific indicator H, prioritising locations where the simulated hydrodynamic processes correspond to the intended function of each intervention.

The geometric mean employed in C2 and C3 limits compensation between components, thereby penalising candidates with a low value in either suitability or hydrodynamic relevance. Candidate scores were normalised separately within each NbS type. During portfolio optimisation, these scores contributed to the combined selection objective, subject to intervention-specific resource targets and spatial compatibility constraints.

The initial candidate counts in Table 2 represent generated geometries rather than the final optimisation-eligible sets. Following common eligibility and data-completeness checks, 733 of the 958 restoration candidates and 9 of the 19 detention-pond candidates remained eligible for C1 and C2. In C3, the additional exclusion of candidates with structurally zero H further reduced these numbers to 666 and 6, respectively, without affecting check-dam or riparian-buffer eligibility. Thus, C1 and C2 differed only in scoring, whereas C3 differed in both scoring and final eligibility.

To distinguish the effects of mechanism-specific scoring and the additional zero-H eligibility restriction, a controlled configuration, C3-unfiltered (C3U), was introduced. C3U repeated the C3 portfolio optimisation while retaining candidates with structurally zero H as eligible, preserving their zero scores without renormalisation. All other selection settings, including candidate scores, resource targets and tolerances, spatial compatibility constraints, lexicographic objectives, and solver settings, remained unchanged. Consequently, C3U and C2 shared an identical eligible candidate pool, while C3U and C3 differed only in the eligibility rule applied during selection. The resulting C3U portfolio was evaluated through two additional hydrodynamic simulations, using the original design and stress-test rainfall events, hydraulic parameters, and numerical settings.

Resource-Constrained Portfolio Optimisation:

To ensure comparable intervention levels across strategies, a common set of resource targets was established before portfolio optimisation. A preliminary feasibility analysis examined the achievable intervention quantities under the available candidate geometries, spatial compatibility rules, and overlap adjustments, without using S, G, H, or strategy-specific scores. The resulting resource targets were specific to the Mandra application and were held constant across the three strategies (Table 4).

Table 4. Common resource targets for the C1–C3 portfolios.

Intervention	Target	Permitted Deviation
Vegetation and soil restoration	400 ha	±5%
Check dams	60 dams	0
Riparian buffers	12 km	±5%
Detention ponds	30,000 m^3	±5%

The common resource targets ensured comparable intervention allocations within predefined tolerances, not identical construction quantities or hydraulic capacities. Although the targets controlled restored area, check-dam count, treated riparian length, and nominal detention storage, the dimensions, composition, and effective hydraulic capacity of the selected interventions remained dependent on their spatial allocation. These differences were quantified through a separate resource-comparability assessment (Section 2.3.2).

The permitted deviations account for the discrete nature of candidate geometries, which prevents exact matching of continuous area, length, and storage-volume targets. The number of check dams was imposed as an exact integer constraint.

Portfolio selection was formulated as a binary integer linear programming problem, in which each candidate intervention i was associated with a binary decision variable x_i, indicating whether the candidate was included in the final portfolio. The optimisation incorporated intervention eligibility, common resource targets, and spatial compatibility constraints.

Spatial conflicts were resolved through predefined rules. Restoration areas and riparian buffers could not overlap, while detention ponds were spatially exclusive of both. Check dams were permitted to intersect restoration or riparian areas, with crest cells removed from the corresponding intervention footprints and resource accounting. Selected check dams

were required to maintain a minimum separation of 200 m along the complete drainage network. Additional minimum separations of 50 m between check dams and detention ponds and 100 m between detention ponds were enforced.

A lexicographic optimisation procedure was adopted to prioritise resource comparability over candidate scores. The successive objectives were to (i) minimise the maximum relative deviation from the four resource targets; (ii) minimise the sum of relative deviations; (iii) minimise total positive target exceedance; and (iv) maximise the resource-weighted strategy-specific score:

$$maxZ_{score} = \sum_{m \in \mathrm{M}} \frac{\lambda_m}{Q_m} \sum_{i \in C_m} \sigma_i r_i x_i \quad (6)$$

where $x_i \in \{0, 1\}$ denotes candidate selection, $\sigma_i \in [0, 1]$ is the strategy-specific score, Q_m is the target quantity for intervention type m, and $\lambda_m = 1$ assigns equal relative importance to the four intervention types. The candidate resource contribution r_i corresponds to effective restoration area (accounting for crest suppression), treated riparian length, nominal detention capacity, or one unit per check dam. Thus, each intervention type contributes its resource-weighted mean score multiplied by its delivered-to-target resource ratio. Subdividing an intervention into smaller units with unchanged total resources and identical scores does not increase the objective value, provided feasibility remains unchanged. Check-dam count was additionally fixed exactly at 60. For C2 and C3, static suitability S served as a second tie-breaking objective of the same resource-weighted form.

The binary integer optimisation problems were solved using HiGHS 1.15.1 through its Python interface (highspy), with a single computational thread and a fixed random seed. Successive lexicographic objectives were preserved using an absolute tolerance of 10^{-7} and a relative tolerance of 10^{-9}. A zero relative MIP-gap target and a time limit of 1800 s were specified for maximum-deviation minimisation, resource-weighted score maximisation, and the static-suitability tie-breaking stage. The intermediate sum-of-deviations and positive-overshoot minimisation stages used a relative MIP-gap tolerance of 10^{-3} and a time limit of 120 s. The solver's default feasibility tolerances (10^{-7} and 10^{-6}) were retained. Consequently, the intermediate refinement stages were not required to achieve proven global optimality.

The optimisation objective was designed to prioritise spatially suitable interventions under predefined resource constraints, rather than to directly minimise inundation extent or building exposure. The candidate scores were not calibrated as predictors of portfolio-level flood mitigation, and no hydrodynamic simulations were performed within the optimisation process. Consequently, the selected portfolios were not assumed to be hydraulically optimal. Their effectiveness was assessed independently through the hydrodynamic simulations described in Section 2.3.

2.3. Hydrodynamic Evaluation and Decision Support

2.3.1. Hydraulic Representation and Experimental Design

Translation of NbS Portfolios into Hydraulic Model Inputs:

The selected C1–C3 portfolios were transferred to the hydrodynamic model as separate spatial configurations, enabling their simulated responses to be compared against the corresponding C0 baseline. For each configuration, the resulting inputs comprised a modified DEM, an elevation-change raster, an intervention-type raster, and spatially distributed target values for Manning's roughness coefficient and the infiltration conductivity-weight parameter. The original grid alignment and NoData mask were preserved, while cells outside the selected intervention footprints retained their baseline properties.

The four NbS types were represented through the following parameter modifications, selected to approximate their intended hydraulic functions at catchment scale. Vegetation

and soil restoration and riparian buffers were modelled by increasing surface roughness and the available infiltration capacity. Minimum target Manning coefficients of 0.16 and 0.18 were applied to restoration and riparian areas, respectively, representing increased vegetation resistance. For both measures, the conductivity-weight parameter was assigned a minimum target value of 1.00. This adjustment removed land-cover-related restrictions on available infiltration without modifying the underlying geology-dependent saturated hydraulic conductivity or other Green–Ampt parameters. Existing parameter values exceeding the prescribed targets were retained.

Check dams were represented by local modifications to the DEM. For each selected structure, a uniform crest elevation was defined 2.0 m above the lowest point of the corresponding channel cross-section. Cells already exceeding this elevation remained unchanged. Flow retention and overtopping were resolved through the two-dimensional OverlandFlow simulation, without introducing separate spillway or outlet structures.

Detention ponds were represented by excavating their interior cells to a target elevation 2.0 m below the corresponding natural spill elevation, without raising the surrounding terrain. The original perimeter and natural overflow elevation were preserved, allowing stored water to infiltrate or overflow along the existing drainage pathway.

Identical parameter values and hydraulic representation rules were applied across C1–C3. Consequently, the configurations differed in the spatial allocation and combination of interventions rather than in the assumed hydraulic behaviour of individual NbS types. These representations were intended for catchment-scale performance assessment rather than detailed engineering design.

The prescribed parameter values represent standardised, screening-level assumptions. The Manning's roughness targets approximate densely vegetated conditions and fall within the upper ranges reported for heavily vegetated floodplains [27,28]. The conductivity-weight target represents an idealised restoration condition rather than a measured increase in soil permeability. Similarly, the 2.0 m structural elevation offsets were adopted as consistent geometric assumptions for preliminary assessment, broadly comparable in scale to small flow-retention and stormwater-storage structures [29,30].

Experimental Design:

The primary hydrodynamic evaluation followed a factorial design comprising four spatial configurations (C0-C3) and the two rainfall events defined in Section 2.1.2, resulting in eight core simulations. The design event (I040_D060) provided the common basis for generating hydrodynamic siting indicators and evaluating the resulting portfolios. The stress event (I070_D060) was used to assess whether the effectiveness and relative performance of the selected portfolios persisted under increased hydrological forcing. All candidate rankings and portfolio selections were based exclusively on information from the C0 design event. The intervention configurations remained unchanged during the stress-test simulations, with no additional siting, optimisation, or hydraulic parameter adjustments. Within each rainfall event, C0-C3 were evaluated under the same forcing and numerical modelling framework.

An additional experiment examined sensitivity to rainfall temporal distribution by comparing the uniform design event with a centre-peaked hyetograph of equal total rainfall (40 mm) and duration (60 min). The alternative hyetograph comprised three successive 20 min intervals with intensities of 27.22, 65.56, and 27.22 mm/h. Four simulations (C0–C3) were performed, retaining the original intervention configurations, hydraulic and numerical settings, and spatially uniform rainfall distribution. Mitigation outcomes were evaluated against the corresponding centre-peaked C0 baseline.

To assess the sensitivity of the simulated mitigation outcomes to hydraulic parameterisation and numerical settings, two additional experiments were conducted under the

design rainfall event, retaining the original intervention locations and spatial footprints. Experiment A adopted a more conservative representation of the NbS interventions by jointly reducing the prescribed hydraulic parameter targets. The minimum Manning's roughness coefficients were reduced from 0.16 to 0.14 for vegetation and soil restoration and from 0.18 to 0.16 for riparian buffers. The minimum infiltration conductivity-weight target for both intervention types was reduced from 1.00 to 0.85, while retaining existing cell values exceeding the prescribed targets. Additionally, the check-dam crest and detention-pond excavation offsets were reduced from 2.0 to 1.5 m. Three simulations (C1–C3) were performed and compared with the unchanged C0 baseline. Experiment B examined numerical time-step sensitivity by reducing the adaptive time-step coefficient α from 0.9 to 0.8, with all other physical parameters unchanged. This required four simulations (C0–C3). In total, seven additional hydrodynamic simulations were conducted. Both experiments used the original rainfall forcing, intervention geometries, evaluation masks, and building-exposure criteria, allowing changes in inundated area and building exposure to be compared with the primary results.

2.3.2. Performance Metrics and Sensitivity Analysis

Flood Performance and Exposure Metrics:

The hydrodynamic performance of each NbS portfolio was evaluated against the corresponding baseline configuration C0 under the same rainfall event. Two primary indicators were adopted: the inundated area exceeding a maximum water depth of 0.10 m and the number of buildings exposed to maximum depths greater than 0.30 m. Additional thresholds of 0.30, 0.50, and 1.00 m were considered to characterise changes across different inundation levels.

To ensure spatial comparability, three nested evaluation masks were established. S1 comprised the 609,395 active (core) nodes of the hydrodynamic model and was used for system-wide quantities, including rainfall, infiltration, and water-balance diagnostics. The difference from the 609,439 valid DEM cells results from 43 outer-edge cells designated as closed (no flow) boundary nodes and one fixed outlet node. These 44 boundary nodes were consistently excluded from the model-output rasters and evaluation masks. The principal evaluation mask, S2′, excluded the union of all cells where the DEM was modified under any intervention configuration (C1–C3). Consequently, the underlying terrain elevation remained identical across configurations within S2′, allowing differences in simulated water depth to be interpreted without interference from direct topographic modifications. A stricter mask, S2, additionally excluded the complete footprints of all selected interventions, including areas where only roughness or infiltration parameters were modified. Both masks were defined consistently across all configurations. The resulting evaluation masks S1, S2′, and S2 comprised 609,395, 608,243, and 534,539 cells, corresponding to approximately 6094.6, 6083.1, and 5346.0 ha, respectively. Thus, S2′ excluded 11.5 ha (0.19% of S1) corresponding to terrain-modified cells, while S2 excluded a further 737.1 ha of intervention footprints, resulting in a total exclusion of 748.6 ha (12.28% of S1). For each simulation, inundated area was calculated from the maximum water depth attained at each computational cell:

$$A(\tau, S) = A_{cell} \cdot N_{exceed}(\tau, S) \quad (7)$$

where $A_{cell} = \Delta x \times \Delta y$ denotes the actual computational cell area (approximately 100.0108 m^2 for the nominal 10 m grid) and $N_{exceed}(\tau,S)$ denotes the number of cells within evaluation mask S for which the maximum simulated water depth exceeds threshold τ. The principal inundation-area indicator was calculated for $\tau = 0.10$ m within S2′.

Building exposure was assessed by sampling maximum water depth at the centroid of each building footprint. To assess spatial sampling sensitivity, exposure was also recalculated using the maximum depth across all grid cells intersecting each building footprint and within a 3 × 3 neighbourhood around its centroid. The original 0.30 m threshold was retained, and each configuration was compared against C0 evaluated using the same sampling method. Exposed buildings were counted separately for each depth threshold, while building-level comparisons identified both reductions in exposure and newly exposed buildings relative to C0. Spatial redistribution was examined through cell-wise differences in maximum water depth, $\Delta h_i = h_{i,\,NbS}^{max} - h_{i,\,C0}^{max}$. Reductions exceeding 0.05 m were classified as improvements, whereas increases exceeding 0.05 m were classified as local worsening. The location of worsening areas was examined relative to detention ponds, check dams, and the predefined urban area, distinguishing local water retention from potentially adverse downstream effects. Maximum flow velocity, mean water depth within intervention zones, and cumulative infiltration were used as diagnostic indicators to interpret the observed changes.

Hydraulic diagnostics were also examined at a model monitoring location where the Agia Aikaterini stream enters the urban area of Mandra. The analysis included local discharge across a monitored 10 m computational cell face, maximum water depth in the surrounding 7 × 7-cell neighbourhood, and additional pond and check-dam pool storage within its topographically delineated contributing area. This location was selected to investigate local flow attenuation and storage behaviour near the urban boundary.

A supplementary resource-comparability assessment examined the realised intervention quantities and storage characteristics of the selected portfolios. Construction-related quantities were derived from the exported intervention geometries and modified terrain rasters. The incremental static detention associated with check dams was estimated through four-connected depression filling of the baseline and crest-modified terrain, while detention-pond utilisation was calculated from simulated water-depth frames at 120 s intervals, considering only water stored below the corresponding natural spill elevations. These quantities were used as model-based indicators of storage potential and utilisation, rather than construction-cost estimates or independently validated field storage capacities.

Sensitivity and Reproducibility Assessment:

Sensitivity analyses addressed candidate scoring, spatial evaluation criteria, rainfall-event severity and temporal rainfall distribution. Scoring robustness was examined using alternative relative weights for geospatial and hydrodynamic information (0.3, 0.5, and 0.7), different normalisation approaches, criterion-removal tests, and alternative assumptions for selected hydrodynamic indicators. Candidate geometries remained fixed during these tests. For each applicable test, ranking stability was evaluated against the corresponding reference ranking using Spearman's rank correlation, and Jaccard overlap for the highest-ranked 25% of candidates.

To further assess portfolio-selection stability, alternative combination weights (w = 0.3 and 0.7, compared to the reference w = 0.5) were propagated through the unchanged portfolio optimisation procedure for C2 and C3. Candidate pools, eligibility rules, resource targets, spatial compatibility constraints, and optimisation settings remained fixed. The alternative selections were compared using candidate retention, Jaccard similarity, resource-weighted overlap, and subcatchment allocation. C1 was not included in this test because its scoring does not depend on w. No additional hydrodynamic simulations were performed for the weight-derived portfolios.

Hydrodynamic evaluation sensitivity was assessed by recalculating the principal spatial indicators using S2 instead of S2′ and repeating the improvement-worsening classification with a depth-change threshold of 0.01 m. Differences in the direction of the estimated effect or the relative ranking of strategies were interpreted as sensitivity to the evaluation assumptions.

Cross-event robustness was assessed by comparing each fixed portfolio under the design and stress-test rainfall events, considering both the magnitude of its effects and changes in the relative performance of C1–C3. Reproducibility checks were performed to assess resource-target compliance, spatial compatibility, and consistency of shared simulation inputs and grid alignment. The resulting resource allocations are reported in Section 3.1. The intervention configurations and model parameters remained fixed throughout the comparative evaluation.

A numerical water-volume balance was also assessed for all eight simulations by comparing changes in surface-water storage with accumulated rainfall, infiltration, outlet discharge, and coastal sink removal. The resulting volume-balance non-closure ranged from −0.040% to +0.072% of the applied rainfall volume. Initial water storage was included in the calculation, while final storage was determined from the instantaneous water-depth fields rather than maximum-depth envelopes. Outlet discharge and coastal sink removal were obtained from the model's accumulated diagnostics and were not independently reconstructed.

2.3.3. Flood Digital Twin Integration

The NbS planning module was implemented as a dedicated scenario-exploration component within the broader Flood Digital Twin research prototype. The prototype also encompasses monitoring-based flood-state estimation and impact-assessment functionalities, which are outside the scope of the present study. The NbS module supports pre-event intervention planning through the spatial visualisation and comparison of precomputed intervention portfolios and their simulated hydraulic outcomes.

The mechanism-specific C3 portfolio is presented as the initial interface configuration to illustrate the most functionally differentiated siting approach, while retaining C1 and C2 as alternative planning strategies. An interactive map combines intervention locations with changes in maximum water depth, building exposure, and selected EO/GIS layers. Summary indicators communicate the expected benefits, residual exposure, and potentially adverse effects associated with each portfolio.

An interactive A/B comparison enables users to examine baseline conditions (C0) alongside the corresponding intervention configuration under the same rainfall event, using consistent visual scales. The interface also supports comparison of each fixed portfolio under the design and stress-test events (Figure 5). The module uses the same evaluation masks, thresholds, and performance indicators as the underlying analysis. It operates independently of real-time scenario recognition and does not rerun candidate selection, optimisation, or hydrodynamic simulations.

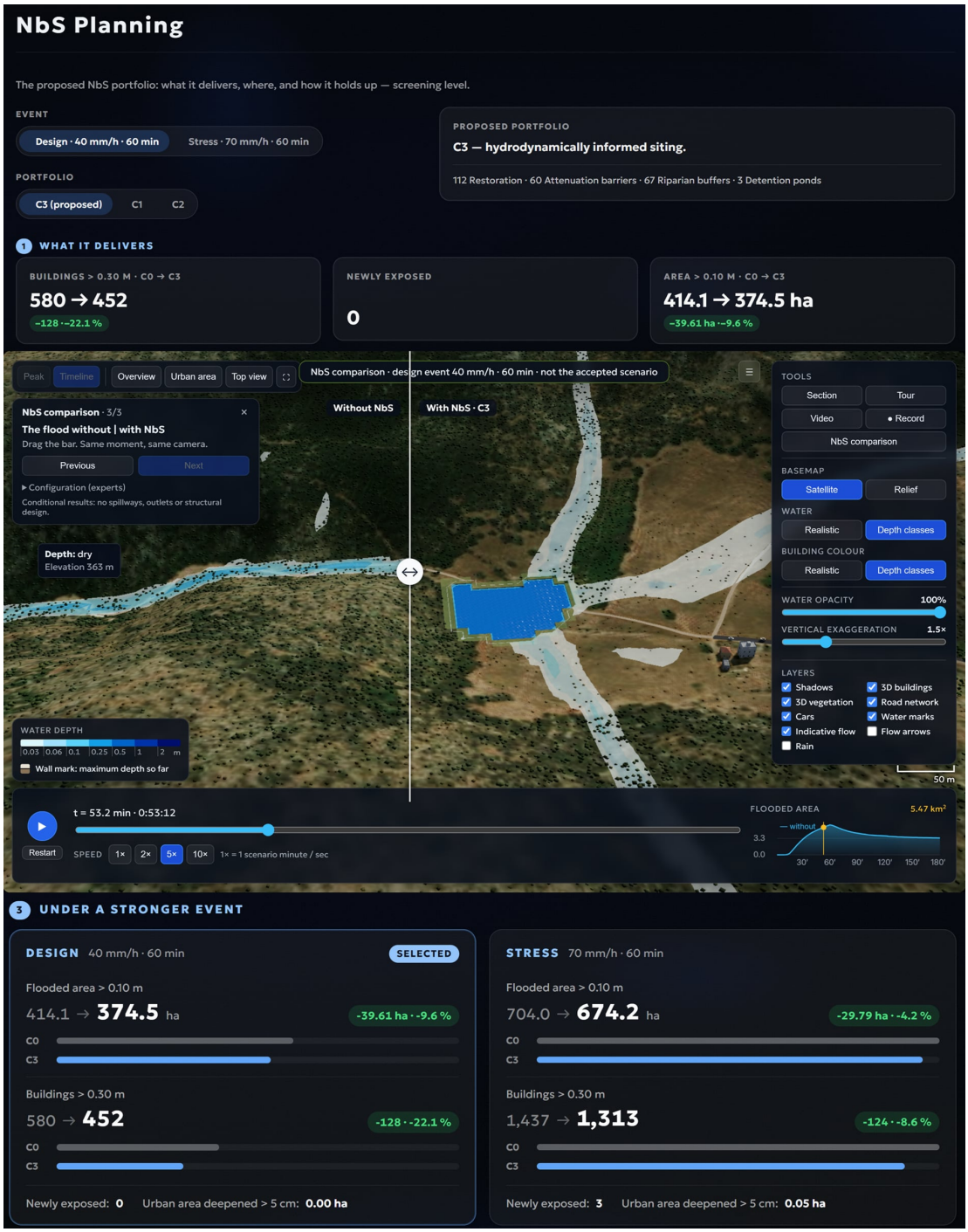

Figure 5. Flood Digital Twin NbS planning interface: intervention portfolio and spatial indicators, and baseline–intervention comparison.

3. Results

3.1. Candidate Ranking and Portfolio Selection

The incorporation of hydrodynamic information altered candidate rankings relative to the static geospatial strategy (C1), although the magnitude of these differences varied across NbS types. Spearman rank correlations between C1 and C2 ranged from 0.653 to 0.875, while those between C1 and C3 ranged from 0.673 to 0.797 (Table 5).

Table 5. Spearman rank correlations between siting strategies and hydrodynamic indicators by NbS type.

NbS Type	C1–C2	C1–C3	C2–C3	G–H
Vegetation and soil restoration	0.653	0.760	0.623	0.148
Check dams	0.875	0.797	0.926	0.845
Riparian buffers	0.824	0.750	0.928	0.817
Detention ponds	0.837	0.673	0.863	0.853

The relationship between general and mechanism-specific hydrodynamic information depended strongly on intervention type. For check dams, riparian buffers, and detention ponds, the correlations between G and H were high (0.817–0.853), and C2 and C3 produced similar candidate rankings (0.863–0.928). In contrast, vegetation and soil restoration exhibited a weaker G–H correlation (0.148) and lower agreement between C2 and C3 (0.623).

The three selection strategies produced distinct intervention portfolios while satisfying the common resource constraints established in Section 2.2.3 (Figure 6).

All configurations included 399.993 ha of vegetation and soil restoration, exactly 60 check dams, and 12 km of riparian interventions. Total detention storage amounted to 29,403.2 m^3 for both C1 and C2 and 29,003.1 m^3 for C3, remaining within the prescribed ±5% tolerance.

Despite these comparable resource allocations, portfolio composition varied. Restoration areas comprised 111 selected units in C1, 106 in C2, and 112 in C3. The corresponding numbers of riparian segments were 64, 65, and 67, while detention storage was distributed across two, five, and three ponds, respectively. The total crest length of the selected check dams also differed, reaching 4020 m in C1, 4200 m in C2, and 4250 m in C3. The lower storage total in C3 reflected its additional eligibility restriction, which excluded ponds with structurally zero mechanism-specific hydrodynamic relevance.

The resource-comparability assessment revealed additional differences in the realised intervention quantities and hydraulic storage characteristics (Table S1 in Supplementary Material). Check-dam crest fill volumes ranged from 38,341 to 40,726 m^3, while detention-pond excavation volumes ranged from 30,116 to 31,851 m^3. Despite increasing total crest lengths from C1 to C3, the estimated static impoundment behind check dams decreased from 246,300 m^3 (C1) to 227,841 m^3 (C2) and 206,422 m^3 (C3). Conversely, under the design rainfall event, peak detention-pond storage within nominal capacity reached 13,801, 20,006, and 27,999 m^3, corresponding to 46.9%, 68.0%, and 96.5% of the available capacity for C1, C2, and C3, respectively. Thus, differences in realised storage potential and utilisation were larger than deviations from the declared resource targets. In particular, larger structural dimensions or nominal storage capacity did not necessarily correspond to greater water retention within the examined configurations.

Spatial differences were more pronounced than variations in total intervention quantities. For vegetation and soil restoration, C1 and C3 exhibited substantial spatial overlap (Jaccard index, J = 0.814), whereas C2 showed lower overlap with either strategy (J = 0.258). Check-dam locations showed more consistent overlap across strategies (J = 0.591–0.631), as did riparian interventions (J = 0.613–0.745). Detention ponds exhibited the greatest spatial divergence, with Jaccard indices ranging from 0.131 to 0.324.

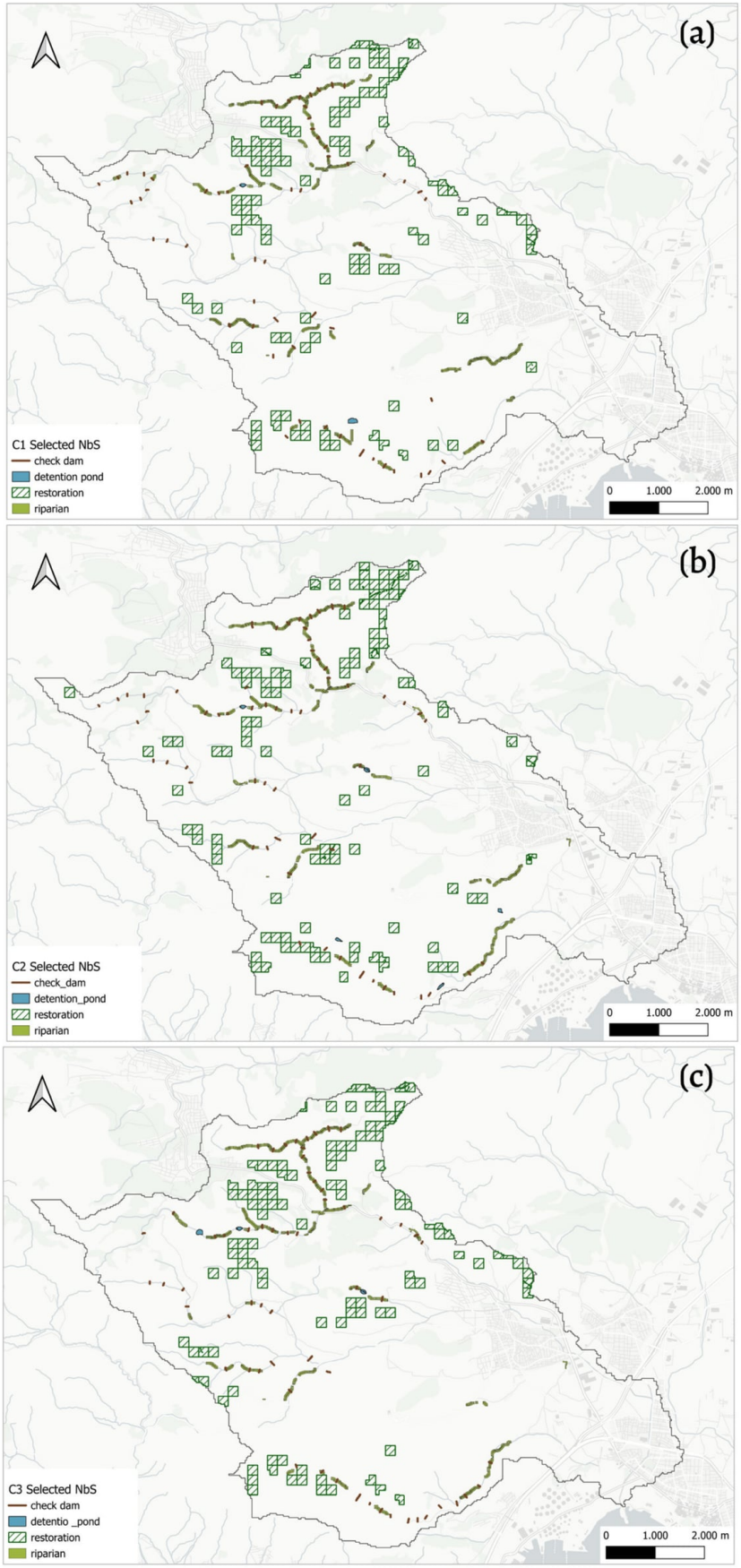

Figure 6. Spatial distribution of selected NbS portfolios: (**a**) C1; (**b**) C2; and (**c**) C3.

3.2. Performance Under the Design Event

Under baseline conditions (C0) of the design event (I040_D060), the inundated area within the principal evaluation mask S2′ reached 414.10 ha for maximum water depths exceeding 0.10 m, 203.58 ha for depths exceeding 0.30 m, and 115.72 ha for depths exceeding 0.50 m.

All three intervention strategies reduced the inundated area across these thresholds (Table 6). For the primary threshold of 0.10 m, the reductions were 36.48 ha (8.81%) for C1, 36.87 ha (8.90%) for C2, and 39.61 ha (9.57%) for C3. C3 achieved the largest reduction, although its advantage over C2 was limited to 2.74 ha. At the 0.30 m threshold, C2 achieved the greatest reduction (37.33 ha), closely followed by C3 (37.10 ha). A similar ordering was observed at 0.50 m, where C2 reduced inundated area by 29.81 ha, compared with 28.95 ha for C3 and 27.54 ha for C1. Considering non-overlapping maximum-depth intervals, C2 increased the inundated area within the 0.10–0.30 m interval by 0.46 ha relative to C0, while reducing the area within the 0.50–1.00 m interval by 30.00 ha.

Table 6. Flooded area and building exposure under the design rainfall event.

Performance Indicator *	C0	C1	C2	C3
Flooded area, h > 0.10 m (ha)	414.10	377.62	377.23	374.49
Flooded area, h > 0.30 m (ha)	203.58	170.23	166.25	166.48
Flooded area, h > 0.50 m (ha)	115.72	88.18	85.91	86.77
Flooded area, h > 1.00 m (ha)	19.48	20.34	19.67	19.52
Buildings, h > 0.30 m (count)	580	467	453	452
Buildings, h > 0.50 m (count)	341	236	227	224

* Note: Flooded areas were calculated within the common S2′ evaluation mask. Building exposure was determined from maximum water depth sampled at building centroids.

Building exposure also decreased under all three strategies. Under baseline conditions, 580 buildings exceeded the primary exposure threshold of 0.30 m. This number decreased to 467 under C1, 453 under C2, and 452 under C3, corresponding to reductions of 19.48%, 21.90%, and 22.07%, respectively. The difference between C2 and C3 was limited to a single building. At the 0.50 m threshold, the number of exposed buildings decreased from 341 under C0 to 236, 227, and 224 under C1, C2, and C3, respectively. Building-level comparisons showed that 113 buildings under C1, 127 under C2, and 128 under C3 moved from above to below the 0.30 m exposure threshold. No previously unexposed buildings crossed above this threshold under any intervention strategy (Figure 7).

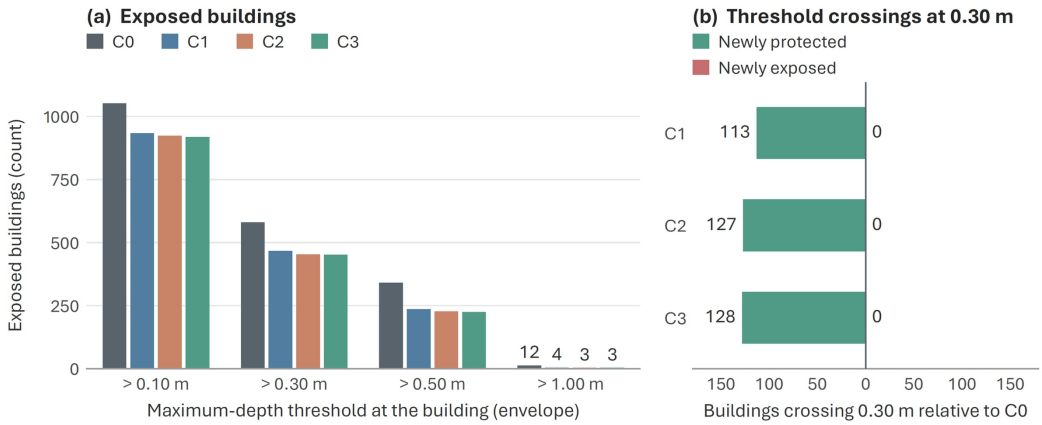

Figure 7. Building exposure under the design event: (**a**) exposed buildings by depth threshold; (**b**) exposure transitions at 0.30 m.

An exception to the overall reduction in inundated area occurred at the highest depth threshold. For depths exceeding 1.00 m, the flooded area increased slightly relative to C0, by 0.86 ha under C1, 0.19 ha under C2, and 0.04 ha under C3. The sensitivity of this result to the spatial evaluation mask is examined in Section 3.5.

3.3. Performance Under the Stress-Test Event

Under baseline conditions (C0) of the stress event (I070_D060), the inundated area within the principal evaluation mask S2′ increased to 703.97 ha for maximum water depths exceeding 0.10 m, 438.56 ha for depths exceeding 0.30 m, and 312.30 ha for depths exceeding 0.50 m. The number of buildings exposed to depths greater than 0.30 m reached 1437.

All three portfolios reduced inundated area across the examined depth thresholds (Table 7). For the primary threshold of 0.10 m, reductions amounted to 32.56 ha (4.63%) under C1, 28.92 ha (4.11%) under C2, and 29.79 ha (4.23%) under C3. Unlike the design event, C1 achieved the largest reduction in this indicator, although the differences between strategies remained small.

Table 7. Flooded area and building exposure under the stress-test rainfall event.

Performance Indicator	C0	C1	C2	C3
Flooded area, h > 0.10 m (ha)	703.97	671.41	675.05	674.18
Flooded area, h > 0.30 m (ha)	438.56	413.53	410.96	412.81
Flooded area, h > 0.50 m (ha)	312.30	294.13	292.35	292.99
Flooded area, h > 1.00 m (ha)	140.08	124.81	123.51	126.11
Buildings, h > 0.30 m (count)	1437	1335	1302	1313

Note: Flooded areas were calculated within the common S2′ evaluation mask. Building exposure was determined from maximum water depth sampled at building centroids.

At higher inundation thresholds, C2 provided the greatest reductions in flooded area. For depths exceeding 0.30 m, the reductions were 25.03 ha under C1, 27.60 ha under C2, and 25.75 ha under C3. C2 also achieved the largest reductions at 0.50 m and 1.00 m. At the latter threshold, all three portfolios reduced flooded area, in contrast to the slight increases recorded under the design event. For the non-overlapping 0.10–0.30 m maximum-depth interval, C1 reduced inundated area by 7.53 ha, compared with 1.32 ha under C2 and 4.04 ha under C3.

Building exposure also decreased under all intervention configurations, although the relative reductions were smaller than those observed for the design event. At the primary threshold of 0.30 m, the number of exposed buildings decreased by 102 (7.10%) under C1, 135 (9.39%) under C2, and 124 (8.63%) under C3.

The net reduction in building exposure was accompanied by a limited number of newly exposed buildings, whereas the design event produced none. At the 0.30 m threshold, 113, 140, and 127 buildings became unexposed under C1, C2, and C3, respectively. Conversely, 11, five, and three buildings, respectively, crossed above the threshold despite remaining below it under baseline conditions (Figure 8).

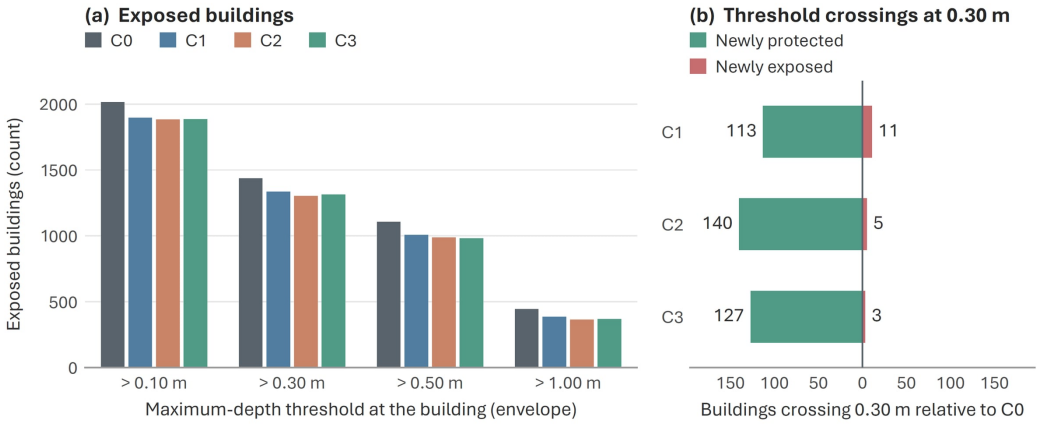

Figure 8. Building exposure under the stress-test event: (**a**) exposed buildings by depth threshold; (**b**) exposure transitions at 0.30 m.

3.4. Spatial Redistribution and Local Effects

The spatial comparison of maximum water-depth fields revealed that the overall reductions in inundation and building exposure were accompanied by both local improvements and increases in flood depth. Using a threshold of 0.05 m for meaningful depth changes, the area experiencing reduced maximum depth was consistently larger than the area experiencing increased depth across all intervention portfolios and both rainfall events (Table 8).

Table 8. Spatial distribution of improved and worsened areas under the design and stress-test events, evaluated within the common S2′ mask.

Event	Strategy	Improved Area (ha)	Worsened Area (ha)	Urban Improvement (ha)	Urban Worsening (ha)
Design	C1	161.15	28.84	27.94	0.00
Design	C2	179.77	28.14	29.43	0.00
Design	C3	172.86	27.08	30.21	0.00
Stress-test	C1	263.77	66.11	7.99	1.46
Stress-test	C2	267.77	69.41	9.45	0.12
Stress-test	C3	266.09	62.88	10.62	0.05

Note: Improvements and worsening correspond to decreases and increases in maximum water depth exceeding 0.05 m relative to C0, respectively. Urban values refer to the intersection of S2′ with the predefined urban area (149.1 ha). The same evaluation mask was applied to all strategies and both rainfall events.

Under the design event, the largest area of reduced maximum depth was obtained with C2 (179.77 ha), whereas C3 produced the smallest area of local worsening (27.08 ha). Within the predefined urban area, all strategies produced depth reductions, covering 27.94–30.21 ha, without any area experiencing an increase greater than 0.05 m.

Under the stress-test event, the spatial extent of both improvements and worsening increased. Areas experiencing reduced maximum depth reached 263.77–267.77 ha, while areas with increased depth reached 62.88–69.41 ha. Limited worsening, absent under the design event, also appeared within the urban area, covering 1.46 ha under C1, 0.12 ha under C2, and 0.05 ha under C3. Nevertheless, urban areas experiencing improvement remained larger than those experiencing worsening in all three configurations.

Figure 9 illustrates these spatial patterns using C3 as a representative configuration. Under both rainfall events, depth reductions were concentrated along major flow pathways and extended towards downstream developed areas. The stress-test event exhibited a more extensive spatial redistribution, including limited adverse changes within the urban domain.

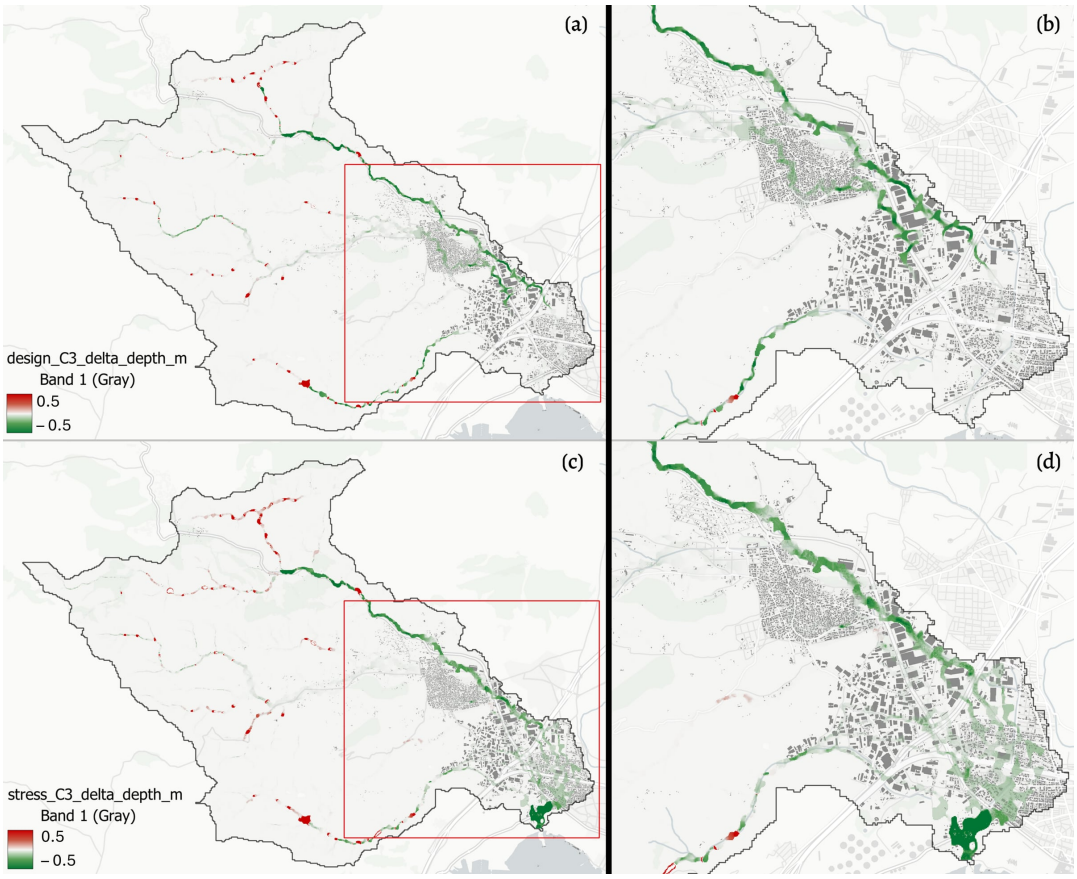

Figure 9. Changes in maximum flood depth (C3-C0) under the (**a**,**b**) design and (**c**,**d**) stress-test events, at catchment and urban scales.

The location of increased depths was examined relative to check dams and detention ponds. Under the design event, 86–90% of the worsened area was located within 200 m of these interventions. Beyond this distance, the affected area was limited to 2.80–4.19 ha. Under the stress-test event, worsening extended further from the intervention locations, with 13.39–24.08 ha occurring beyond 200 m. These spatial associations describe the location of adverse changes but do not establish their individual causes, as the four NbS types were simulated together rather than evaluated independently.

Complementary hydrodynamic indicators provided further information on intervention-zone responses. In riparian zones, the 90th percentile of maximum flow velocity decreased from 1.17–1.27 to 0.78–0.79 m/s under the design event and from 1.65–1.87 to 1.17–1.27 m/s under the stress-test event. In check-dam zones, corresponding velocities decreased from 1.3–1.4 to 1.1 m/s under the design event and from 1.93–2.02 to 1.63–1.70 m/s under the stress-test event. These reductions were accompanied by increases in mean water depth relative to C0 of 0.24–0.27 m and approximately 0.30 m, respectively, consistent with local flow retention. For each portfolio, baseline values were evaluated over its corresponding intervention zones. Total cumulative infiltration also increased under all portfolios, by 22,300–22,600 m^3 (1.44–1.46%) under the design event and 12,862–14,601 m^3 (0.70–0.80%) under the stress-test event.

Diagnostics at the Agia Aikaterini urban-entry monitoring location provided evidence of local flow attenuation and storage-related effects (Figure 10). Under the design event, the NbS portfolios reduced peak local cell-face discharge by 11.3–13.9% and delayed its occurrence by approximately 15–16 min relative to C0. Additional water stored within detention ponds and check-dam pools in the contributing drainage area reached 22–28 × 10^3 m^3 at the end of rainfall and 33–43 × 10^3 m^3 by the end of the simulation. The local depth response

showed a corresponding attenuation and delay. Under the stress-test event, peak attenuation was less pronounced and less reliably resolved, while late-time discharge slightly exceeded C0.

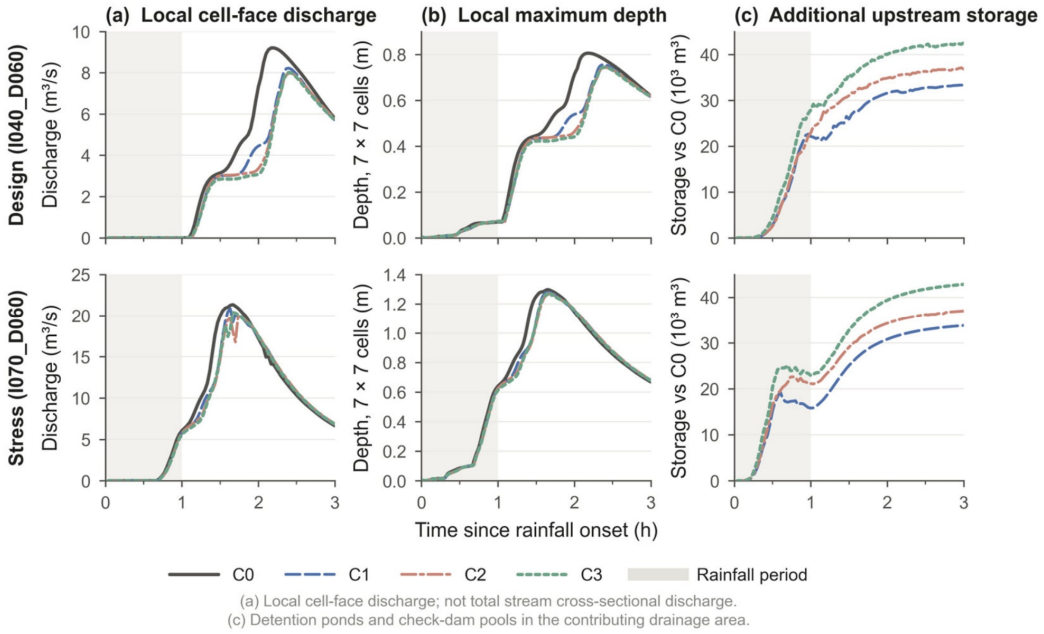

Figure 10. Local hydraulic diagnostics at the Agia Aikaterini stream entrance to the urban area of Mandra under the design (upper row) and stress-test (lower row) rainfall events: (**a**) discharge through a monitored 10 m computational cell face; (**b**) maximum water depth within the surrounding 7 × 7-cell neighbourhood; and (**c**) detention-pond and check-dam pool storage relative to C0.

3.5. Cross-Event Performance and Sensitivity

Under increased rainfall intensity, all three NbS portfolios maintained a beneficial effect, but both the magnitude of improvement and the relative ranking of strategies changed. All portfolios reduced inundated area at thresholds up to 0.50 m and building exposure across the examined thresholds under both events. However, reductions in inundated area exceeding 0.10 m decreased from 8.81 to 9.57% under the design event to 4.11–4.63% under the stress-test event. Similarly, reductions in building exposure exceeding 0.30 m decreased from 19.48 to 22.07% to 7.10–9.39%.

The relative performance of the strategies was event-dependent. Under the design event, C3 achieved the greatest reduction in both primary indicators: inundated area exceeding 0.10 m and buildings exposed to depths exceeding 0.30 m. Under the stress-test event, however, C1 achieved the largest reduction in the former, whereas C2 performed best in the latter. A further distinction occurred at the 1.00 m inundation threshold, where all three strategies produced small area increases under the design event but substantial reductions under the stress-test event.

The sensitivity of these comparisons to the spatial evaluation mask was also examined (Figure 11). Under the stress-test event, the ranking for inundated area exceeding 0.10 m changed from C1 > C3 > C2 within the primary mask S2′ to C2 > C1 > C3 within the stricter mask S2. Nevertheless, all three strategies continued to reduce inundated area under both masks. Under the design event, the ranking remained C3 > C2 > C1, although the difference between C3 and C2 decreased to only 0.12 ha within S2. At the 1.00 m threshold, mask selection also affected the direction of the estimated change under the design event: the slight increases observed within S2′ became reductions when the complete intervention footprints were excluded.

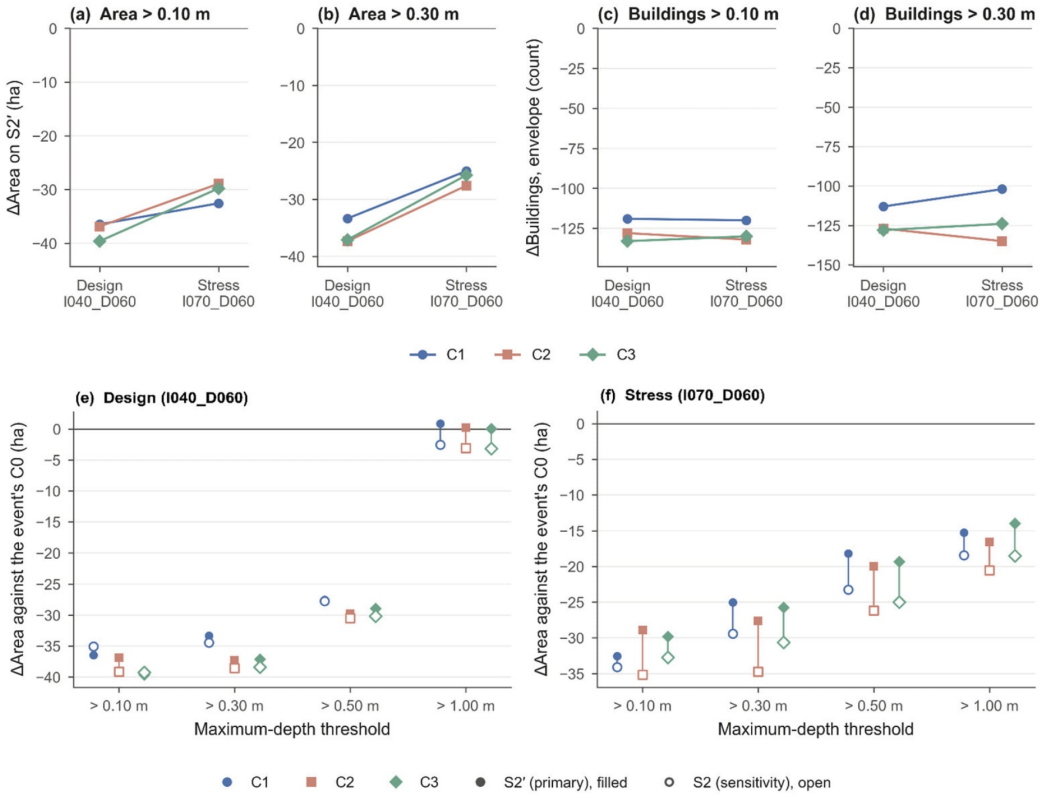

Figure 11. Cross-event flood-performance changes (**a**–**d**) and evaluation-mask sensitivity under the (**e**) design and (**f**) stress-test events. Negative values indicate reductions relative to C0.

The classification of spatial improvement and worsening was also sensitive to the selected depth-change threshold. Reducing the threshold from 0.05 to 0.01 m increased the areas classified as both improved and worsened. Although improved areas remained more extensive than worsened areas, their absolute values and the relative ranking of strategies varied.

Alternative building-exposure sampling methods increased absolute exposure counts by 26–41% (footprint maximum) and 34–61% (3 × 3 neighbourhood maximum) relative to centroid sampling. Under every sampling method, all portfolios reduced exposure relative to their corresponding C0 baseline, and the nominal strategy ordering remained unchanged (design: C3 > C2 > C1; stress: C2 > C3 > C1). The small design-event difference between C2 and C3 remained sensitive to the sampling method and did not establish a robust performance distinction.

Experiments A and B examined the influence of intervention parameterisation and numerical time stepping on the primary flood-mitigation indicators (Table 9). Under the more conservative NbS representation (Experiment A), all three portfolios continued to reduce inundated area and building exposure, although the magnitude of the benefits decreased. Reductions in inundated area exceeding 0.10 m ranged from 6.4% to 6.7%, compared with 8.8–9.6% in the primary simulations, while reductions in building exposure above 0.30 m decreased to 11.6–13.1%, compared with 19.5–22.1%. Differences among strategies narrowed to at most 1.2 ha and nine buildings. C3 retained the largest reduction in both primary indicators, whereas C1 and C2 exchanged positions for inundated area. Under the alternative numerical setting (Experiment B, $\alpha = 0.8$), reduction rates differed from the original simulations by at most 0.3 percentage points for inundated area and 1.9 percentage points for building exposure, without changing the relative strategy rankings. However, numerical variations of up to 12 exposed buildings per configuration exceeded some of the original inter-strategy differences, particularly the one-building difference between C2

and C3. Overall, the direction of the mitigation benefits remained consistent, whereas their magnitude and the significance of small differences among strategies were sensitive to the tested assumptions.

Table 9. Sensitivity of flood-mitigation performance to intervention parameterisation and numerical time-step settings under the design rainfall event.

Simulation Set	Inundated-Area Reduction	Building-Exposure Reduction	Main Observation
Primary simulations ($\alpha = 0.9$)	8.81–9.57%	19.48–22.07%	C3 achieved the greatest numerical reductions
Exp. A—Conservative NbS representation	6.4–6.7%	11.6–13.1%	C3 remained first; differences ≤ 1.2 ha and ≤9 buildings
Exp. B—Reduced time-step coefficient ($\alpha = 0.8$)	Change ≤0.3 percentage points	Change ≤1.9 percentage points	Strategy rankings unchanged

Note: Inundated-area reductions refer to maximum depths exceeding 0.10 m within S2′; building-exposure reductions refer to centroid-sampled maximum depths exceeding 0.30 m. Values for the primary simulations and Experiment A represent ranges across C1–C3. Experiment B reports the maximum absolute change in reduction rates relative to the corresponding primary simulations. Experiment A comprised three additional runs (C1–C3) evaluated against the unchanged C0 baseline. Experiment B comprised four additional runs (C0–C3).

The controlled C3U experiment examined the separate contributions of mechanism-specific scoring and zero-H candidate exclusion to the observed C2–C3 performance differences (Table 10). Under common eligibility, C3U achieved greater reductions in inundated area than C2 by 3.61 ha under the design event and 1.58 ha under the stress-test event, but resulted in three and eight additional exposed buildings, respectively. Compared with C3U, the original zero-H exclusion in C3 reduced the design-event building exposure by four buildings but decreased the inundated-area reduction by 0.87 ha. Under the stress-test event, the exclusion reduced the inundated-area benefit by 0.71 ha and increased building exposure by three buildings. The eligibility change also affected portfolio composition: C3U selected two zero-H detention ponds, allowing a closer match to the nominal storage target (29,403.2 m^3 compared with 29,003.1 m^3 in C3). Overall, the controlled results showed that mechanism-specific scoring provided modest, metric-dependent differences, while zero-H exclusion did not produce a consistent additional hydraulic benefit.

The temporal-distribution experiment showed that concentrating the same nominal rainfall within the central part of the storm altered the simulated flood response (Table 11). Under C0, inundated area increased from 414.10 to 469.23 ha, while exposed buildings increased from 580 to 608. All three fixed NbS portfolios maintained beneficial effects, with inundated-area reductions of 51.93–53.61 ha (11.07–11.42%), compared with 36.48–39.61 ha (8.81–9.57%) under uniform rainfall. Conversely, building-exposure reductions decreased from 113 to 128 buildings (19.48–22.07%) to 102–120 buildings (16.78–19.74%). The nominal ranking C3 > C2 > C1 remained unchanged for both primary indicators, although the differences between adjacent strategies varied. Spatially, 94.6–95.7% of the area improved under uniform rainfall remained improved under the centre-peaked event, with very limited reversals between improvement and worsening.

Table 10. Controlled comparison of mechanism-specific scoring and zero-H eligibility restriction, expressed as differences in flood-impact reductions relative to C0.

Event	Comparison	Difference in Flooded-Area Reduction	Difference in Building-Exposure Reduction
Design	C3U − C2 (scoring)	+3.61 ha (+0.87 pp)	−3 (−0.52 pp)
Design	C3 − C3U (zero-H exclusion)	−0.87 ha (−0.21 pp)	+4 (+0.69 pp)
Design	C3 − C2 (original comparison)	+2.74 ha (+0.66 pp)	+1 (+0.17 pp)
Stress-test	C3U − C2 (scoring)	+1.58 ha (+0.22 pp)	−8 (−0.56 pp)
Stress-test	C3 − C3U (zero-H exclusion)	−0.71 ha (−0.10 pp)	−3 (−0.21 pp)
Stress-test	C3 − C2 (original comparison)	+0.87 ha (+0.12 pp)	−11 (−0.77 pp)

Note: Differences represent the reduction achieved by the first configuration minus that achieved by the second, relative to the corresponding C0 baseline. Positive values indicate greater mitigation by the first configuration. Inundated area was evaluated at h > 0.10 m within S2′, and building exposure at centroid-sampled maximum depth > 0.30 m. pp denotes percentage points.

Table 11. Flood-mitigation performance under the centre-peaked design rainfall, compared with the event-specific baseline C0.

Configuration	Flooded Area (ha)	Area Reduction (ha; %)	Exposed Buildings	Building Reduction (n; %)
C0	469.23	-	608	-
C1	417.30	51.93 (11.07%)	506	102 (16.78%)
C2	417.03	52.20 (11.12%)	501	107 (17.60%)
C3	415.62	53.61 (11.42%)	488	120 (19.74%)

Note: The centre-peaked event applied 27.22, 65.56, and 27.22 mm/h over successive 20 min intervals. Flooded area was defined by maximum depth > 0.10 m within S2′, and building exposure by centroid-sampled maximum depth > 0.30 m. Reductions were calculated relative to the centre-peaked C0.

Candidate-scoring sensitivity was assessed separately from hydrodynamic performance. Of 171 planned comparisons, 168 were applicable. Across most alternative parameterisations, candidate rankings remained stable, with median Spearman correlations ranging from 0.944 to 1.000. The greatest deviations occurred in leave-one-criterion-out tests, particularly for vegetation and soil restoration. The lowest correlation was observed for C1 following removal of median NDVI ($\rho = 0.677$). For the highest-ranked 25% of candidates, minimum Jaccard overlap reached 0.375, while median values across the evaluated cases ranged from 0.667 to 1.000.

The portfolio-selection sensitivity analysis showed that ranking stability did not necessarily translate into identical intervention selections (Table 12). Under the alternative weighting configurations, C3 retained 97% of its original restoration area, 85–87% of its check dams, 91–92% of its riparian treated length, and all selected detention ponds. C2 exhibited greater sensitivity, retaining 75–78% of its restoration area and 83–88% of its check dams. At w = 0.3, four smaller detention ponds were replaced by a single larger pond, while total nominal storage capacity remained unchanged. All alternative portfolios satisfied the same resource targets as their reference configurations, and most spatial reallocations remained within comparable subcatchment areas. This occurs particularly where discrete intervention combinations and spatial constraints influence selection.

Table 12. Resource-weighted retention of original NbS selections under alternative scoring weights.

Strategy	Weight (w)	Restoration Area	Check Dams	Riparian Length	Pond Capacity
C2	0.3	75%	88%	90%	22%
C2	0.7	78%	83%	94%	100%
C3	0.3	97%	87%	91%	100%
C3	0.7	97%	85%	92%	100%

Note: Values represent the proportion of the original selected resource retained at the same locations (selected-unit retention for check dams). The reference weight was w = 0.5. Resource targets and total delivered quantities were unchanged across the tested configurations. A low retention percentage does not imply a reduction in total allocated resources.

4. Discussion

4.1. Added Value of Flood-Dynamics-Informed Siting

All three NbS portfolios reduced the two primary simulated flood-impact indicators relative to C0 under both rainfall events. Differences among C1–C3 (at most 2.6 percentage points for building exposure and 0.8 percentage points for inundated area) were much smaller than their improvements relative to baseline (7–22% and 4–10%, respectively), indicating broadly comparable performance among the examined strategies. However, this comparison does not isolate the relative contributions of intervention implementation and spatial prioritisation, as all three portfolios were generated through systematic siting procedures.

The static EO/GIS-based strategy (C1) provided a relevant benchmark: it remained competitive across several indicators and achieved the greatest reduction in inundated area exceeding 0.10 m under the stress-test event. A systematic combination of land-cover compatibility, terrain characteristics, and spatial eligibility constraints can therefore already support effective preliminary NbS planning, and the results do not support treating static geospatial suitability as an inherently inadequate planning approach.

Nevertheless, incorporating hydrodynamic information introduced distinctions that static suitability alone did not capture. Both C2 and C3 altered candidate rankings and produced spatially different intervention portfolios despite starting from the same initial candidate geometries and operating under comparable resource constraints. This reflects the difference between identifying where an intervention is physically suitable and identifying where its placement is relevant to the simulated flood dynamics.

Under the design event, both hydrodynamically informed strategies achieved greater reductions in the principal inundation and building-exposure indicators than C1. Under the stress-test event, C2 retained an advantage in reducing building exposure, whereas C1's advantage in inundated area exceeding 0.10 m was confined to the shallowest depth class (Section 4.3). Additional hydrodynamic information was therefore associated with modest gains for selected objectives rather than universally superior portfolios.

The targeted sensitivity experiments further showed that, although the direction of the mitigation benefits remained consistent, their magnitude depended on the assumed hydraulic representation of the interventions. Moreover, the small differences among strategies were comparable to variations introduced by the numerical settings. Consequently, the observed rankings should be interpreted as indicative outcomes of the examined configurations and not as robust evidence of one siting strategy consistently outperforming the others.

These findings are consistent with previous research emphasising runoff-source identification, hydrological connectivity, and the integration of hydraulic indicators into NbS prioritisation [7,8,31]. The contribution of the present study lies primarily in the struc-

tured comparison of three siting strategies, using a shared initial candidate space and comparable intervention-resource constraints, followed by hydrodynamic evaluation of the selected portfolios.

An important distinction concerns the relationship between suitability-based optimisation and hydraulic effectiveness. The optimisation favoured candidates according to predefined geospatial and hydrodynamic relevance indicators, yet all three resulting portfolios reduced both primary flood-impact indicators under the examined rainfall events and in the hydraulic sensitivity experiments. This shows that the proposed screening and selection procedure can identify portfolios with beneficial simulated outcomes under the tested conditions, but does not establish that the suitability scores reliably predict the magnitude of flood mitigation or that the selected portfolios are hydraulically optimal. In particular, the relatively small performance differences among spatially distinct portfolios indicate that higher informational complexity or different suitability-based priorities do not necessarily translate into proportionally greater hydraulic benefits.

4.2. Mechanism-Specific Siting and Event Dependence

The distinction between general and mechanism-specific hydrodynamic information is particularly relevant to NbS planning, as locations exhibiting intense flooding are not necessarily those where a particular intervention can most effectively influence the underlying processes. While the general indicator G characterises flood activity through water depth and discharge, the mechanism-specific indicator H links candidate prioritisation to runoff generation, flow-path attenuation, or temporary storage, depending on the intended function of each measure.

The results suggest that this functional differentiation does not contribute equally across intervention types. For check dams, riparian buffers, and detention ponds, general and mechanism-specific hydrodynamic indicators were strongly correlated ($\rho = 0.817$–0.853), indicating that general flood activity already captured much of the spatial information represented by their specialised criteria. In contrast, vegetation and soil restoration exhibited a weaker relationship ($\rho = 0.148$). This difference reflects the distinction between local runoff generation and the accumulation or conveyance of water originating elsewhere in the catchment. Consequently, mechanism-specific scoring changed prioritisation most for vegetation and soil restoration, the only intervention type targeting runoff generation.

Under the design event, C3 achieved the greatest numerical improvement in both primary performance indicators, the largest urban area of depth reduction (30.21 ha), and the smallest area of local worsening (27.08 ha). However, its advantage over C2 was limited (2.74 ha and one building under the design event), particularly for building exposure, and did not persist under the stress-test event. Differences in this size cannot be interpreted as evidence that one strategy outperforms another. Increasing the functional specificity of siting criteria therefore did not guarantee consistently greater hydrodynamic effectiveness.

The hydrodynamic indicators used for siting were derived exclusively from the baseline design event. The selected portfolios retained beneficial effects under stronger rainfall forcing, but their relative performance changed. Intervention portfolios should be evaluated across multiple hydrological conditions since a configuration performing best under its design event may not remain preferable under more severe conditions.

The temporal-distribution experiment showed that rainfall-event dependence extends beyond differences in total rainfall or intensity. Concentrating the design rainfall into a central peak increased baseline inundation, particularly near the margins of the flooded area, where the NbS portfolios produced greater relative reductions in inundation extent. Building-exposure benefits, however, decreased despite the broadly preserved spatial pattern of flood mitigation. This difference was largely associated with threshold crossings

under the deeper baseline flood: many buildings previously protected below 0.30 m remained subject to similar depth reductions but exceeded the exposure threshold under the centre-peaked event. A smaller proportion experienced an actual weakening of the simulated depth reduction. Although the nominal ordering of the three strategies was preserved, the differences between adjacent portfolios remained sensitive to rainfall forcing and were often comparable to the model's numerical sensitivity. The results therefore support the qualitative persistence of mitigation benefits under the tested temporal redistribution, but not a general conclusion of robust quantitative superiority across alternative rainfall patterns.

The original comparison between C2 and C3 combined two methodological differences: hydrodynamic scoring and candidate eligibility. The C3U experiment separated their effects at the level of the portfolio-selection procedure. With identical eligible candidate pools, mechanism-specific scoring produced slightly greater inundated-area reductions than general hydrodynamic scoring under both rainfall events, but did not improve building exposure. Conversely, excluding structurally zero-H candidates provided no consistent additional benefit and partly offset the inundated-area improvements associated with mechanism-specific scoring. The one-building advantage of the original C3 over C2 under the design event depended on this eligibility restriction, whereas its inundated-area advantage remained when eligibility was held constant. The added value of more specialised hydrodynamic information is metric-dependent, while additional eligibility restrictions may alter portfolio composition without yielding greater hydraulic effectiveness. Since the controlled comparisons involve different optimised portfolios, their effects reflect changes in the selection rules and resulting spatial allocations.

4.3. Inundation Extent and Local Depth Increases

Inundation extent above 0.10 m does not distinguish shallow from deep flooding, and a smaller reduction in extent does not necessarily indicate a less effective portfolio. Under the stress-test event, C1's advantage in this indicator was concentrated in the 0.10–0.30 m depth class, whereas C2 achieved greater reductions at higher depth thresholds and in building exposure. Under the design event, C2's reduction in the deeper 0.50–1.00 m class co-existed with a small increase in the shallower 0.10–0.30 m class. These patterns show that strategy rankings depend on the depth ranges considered.

Local depth increases require a similar distinction. Check dams and detention ponds act through local retention and temporary storage (Section 2.2.1), and increased depths in their vicinity partly reflect this intended function. Under the design event, 86–90% of the worsened area lay within 200 m of these structures, no worsening occurred within the urban area, and mean water depths in check-dam zones increased while velocities decreased (Section 3.4). The evaluation masks support this interpretation: the slight increases in area deeper than 1.00 m under the design event became reductions once the complete intervention footprints were excluded, and under the stress-test event C2 achieved the largest reduction in inundated area within S2 (Section 3.5). Part of the apparent performance loss within S2′ therefore arises from water held within or near the interventions. This interpretation applies only where the retained water does not reach buildings or infrastructure.

The local discharge and storage diagnostics further support an attenuation-and-delay response associated with upstream water retention under the design event, with weaker attenuation under more severe rainfall. However, these findings concern a single monitoring location and cannot isolate the contributions of individual NbS types or establish the hydraulic response of the entire drainage network.

Not all increases can be attributed to intended retention. Under the stress-test event, 13.39–24.08 ha of worsening occurred more than 200 m from check dams and ponds, wors-

ening appeared within the urban area (0.05–1.46 ha), and 3–11 buildings became newly exposed. These effects remain adverse and show that portfolios selected for the design event can redistribute flooding under stronger forcing. Extent-based indicators should therefore be read together with depth classes, building exposure, and the location of depth increases relative to the interventions and the urban area.

4.4. Digital Twin Integration and Decision-Support Implications

Integrating the proposed siting framework into the Flood Digital Twin enables the spatially explicit comparison and interpretation of alternative intervention portfolios. By linking the selected portfolios with their simulated effects on inundation, building exposure, and residual flood conditions, the NbS planning module provides a basis for examining alternative planning decisions.

The results indicate that intervention performance cannot be adequately represented by a single aggregate indicator. The differences between strategies, particularly under the stress-test event, show that overall flood reduction needs to be considered alongside local worsening, newly exposed buildings, and performance under different rainfall conditions. The Digital Twin supports this multidimensional assessment by enabling consistent baseline–intervention comparisons and spatial exploration of the corresponding hydrodynamic outcomes.

C3 is displayed initially to illustrate mechanism-specific hydrodynamic prioritisation. The observed differences among strategies and their event-dependent rankings prevent recommending any single portfolio based on the present results alone. The interface therefore retains C1 and C2 as equally accessible alternatives, allowing users to examine trade-offs across intervention locations, inundation extent, building exposure, and local adverse effects.

The current NbS module is an offline, scenario-based planning component that presents precomputed intervention portfolios and their evaluated hydrodynamic outcomes without performing interactive optimisation or new simulations. Although the main computational stages were implemented in code, the workflow still required expert visual inspection to identify and resolve problematic intervention geometries and inconsistencies in raster-derived inputs and outputs. Enabling fully automated, on-demand NbS generation, portfolio selection, and hydraulic evaluation within the Digital Twin would therefore require robust quality-control and error-handling procedures, as well as validation of the complete workflow without manual intervention. Such an extension represents a distinct methodological development beyond the scope of the present study.

4.5. Limitations and Transferability

The findings should be interpreted within the scope of a deterministic, screening-level assessment. Each intervention configuration was simulated once per rainfall event, so small performance differences between strategies, particularly those involving only a few hectares or buildings, represent numerical outcomes of the examined simulations. Strategy rankings were sensitive to the evaluation mask and depth-change threshold (Section 3.5), and the hydraulic sensitivity experiments showed that the magnitude of the estimated mitigation benefits also depended on intervention parameterisation. These experiments examined two targeted alternative settings rather than a comprehensive parameter ensemble and do not establish the full uncertainty range of the simulated outcomes.

The analysis was restricted to a single catchment, two uniform-intensity rainfall scenarios, and one additional centre-peaked temporal distribution of the design event. Although these experiments provide a focused test of rainfall severity and temporal distribution, they

do not establish performance across different catchments, spatial and temporal rainfall distributions, or hydroclimatic conditions.

The hydraulic representation of NbS interventions was intended for preliminary spatial planning rather than detailed engineering design. Check dams and detention ponds were represented through simplified terrain modifications, while vegetation-related measures were modelled through changes in surface roughness and infiltration parameters. The eventual classification of check dams and detention ponds as nature-based or hybrid solutions would depend on site-specific design and implementation. Site-specific considerations, including land ownership, existing infrastructure, construction accessibility, permitting requirements, and social acceptance, were not incorporated into the final selection process. The resulting locations should therefore be regarded as preliminary intervention candidates requiring further feasibility assessment. Building exposure remains a screening-level indicator, as alternative spatial sampling methods substantially changed absolute exposure counts, although the relative strategy ordering was preserved; none of these methods provides validated building-level flood depths.

Although the portfolios were selected under common resource targets, they were not physically or hydraulically equivalent. Differences in intervention dimensions, composition, excavation volumes, and storage characteristics arose alongside changes in spatial allocation. These differences may have contributed to the observed hydrodynamic responses, but their independent effects cannot be isolated because intervention quantities and locations varied simultaneously. Consequently, the comparisons should be interpreted as the performance of alternative siting strategies under comparable declared resource allocations, and not as a controlled assessment of hydraulically identical interventions.

An additional limitation concerns the infiltration formulation, which does not impose an explicit maximum soil-profile storage capacity. Although infiltration is constrained by the available surface water and the Green–Ampt hydraulic parameters, the absence of a finite storage limit may overestimate the sustained infiltration benefits of restoration measures, particularly under prolonged rainfall or where the effective soil depth is limited. Experiment A examined the sensitivity to a more conservative infiltration-related parameterisation, but did not explicitly introduce a finite soil-storage constraint. Therefore, the potential influence of soil-storage limitations remains unquantified and should be considered when interpreting the estimated benefits of infiltration-based interventions.

Furthermore, hydrodynamic performance was evaluated for complete portfolios, not for individual NbS types. The contribution of each intervention mechanism to the overall flood response cannot therefore be isolated.

Although candidate rankings remained strongly correlated across the tested weighting configurations, portfolio-level stability varied between strategies and intervention types. C3 exhibited relatively high selection stability, whereas C2 showed greater sensitivity, particularly in detention-pond selection. This confirms that ranking stability alone is insufficient to establish portfolio stability. Furthermore, the weight-derived portfolios were not evaluated hydrodynamically: the hydraulic sensitivity experiments reported in this study concern the original portfolios under alternative modelling settings and rainfall forcing. Consequently, the hydraulic performance of the weight-derived portfolios and the persistence of relative strategy rankings under changes in scoring weights remain unverified.

Although evaluated in a single catchment, the proposed planning workflow is structured for adaptation to other study areas. The separation of spatial eligibility from suitability scoring, the generation of a common candidate space, the subsequent integration of flood-dynamics information, and the comparison of alternative portfolios under predefined resource constraints constitute a transparent and reproducible planning procedure. Appli-

cation to other catchments would require locally appropriate geospatial and hydrodynamic inputs, intervention-specific constraints, and independent performance evaluation.

5. Conclusions

This study developed and evaluated an integrated computational workflow for preliminary NbS planning, linking EO/GIS-based candidate generation, hydrodynamic siting indicators, resource-constrained portfolio optimisation, and hydraulic performance assessment. Applied to the Mandra catchment, Greece, the framework compared three strategies under common intervention-resource targets: static EO/GIS suitability (C1), suitability combined with general hydrodynamic indicators (C2), and suitability combined with mechanism-specific hydrodynamic indicators (C3). The selected portfolios were evaluated under 40 mm/h design and 70 mm/h stress-test rainfall events, each lasting 60 min. The findings address three research questions.

First, incorporating simulated flood dynamics altered candidate prioritisation and the spatial composition of selected NbS portfolios. Compared with static EO/GIS suitability (C1), hydrodynamically informed strategies (C2 and C3) achieved slightly greater reductions in building exposure under both rainfall events (by 1.5–2.6 percentage points). However, these improvements depended on the performance indicator, as C1 achieved the largest reduction in inundated area exceeding 0.10 m under the stress-test event. Given the small size of these gains and the deterministic design, the resulting strategy rankings are indicative.

Second, matching hydrodynamic indicators to the functional mechanisms of individual NbS types produced distinct siting priorities, particularly for vegetation and soil restoration, where general and mechanism-specific indicators showed weak agreement ($\rho = 0.148$). Although C3 achieved the greatest numerical reductions in the two primary performance indicators under the design event, its advantage over C2 was small and did not persist under stronger rainfall. Moreover, because C3 also modified final candidate eligibility, the observed differences cannot be attributed only to mechanism-specific scoring.

Third, all three portfolios maintained reductions in the primary inundation-area and building-exposure indicators under the more intense rainfall event, although their relative rankings changed. Inundated-area reductions ranged from 4.11% to 4.63% (compared with 8.81–9.57% under the design event), while reductions in exposed buildings ranged from 7.10% to 9.39% (compared with 19.48–22.07%). Local depth increases occurred near check dams and detention ponds, consistent with intended retention, but under the stress-test event some increases occurred more than 200 m from these structures and reached the urban area, while 3–11 buildings became newly exposed. The alternative temporal distribution of the design storm likewise preserved the overall mitigation benefits, although their magnitude and the differences between strategies remained sensitive to rainfall forcing.

The integration into the Flood Digital Twin demonstrated the feasibility of bringing alternative NbS portfolios and their precomputed hydrodynamic outcomes into a spatially explicit planning environment. Such an environment is relevant given the observed trade-offs between inundation extent, building exposure, and local adverse effects, which highlight the limitations of relying on a single performance indicator when comparing intervention strategies. While the resulting module enables interactive examination of these differences, it does not yet provide fully automated NbS planning. Achieving on-demand portfolio generation and evaluation would require further development and validation of automated quality-control procedures, as intervention geometries and geospatial inputs still require expert inspection in the present workflow.

The principal contribution of this work is a structured and reproducible framework for comparing alternative NbS siting strategies using a shared initial candidate space,

comparable intervention resources, and consistent portfolio-level hydrodynamic evaluation. Although the quantitative findings are specific to the examined catchment and rainfall conditions, the methodological workflow provides a basis for adaptation to other flood-prone areas.

Supplementary Materials: The following supporting information can be downloaded at: https://www.mdpi.com/article/10.3390/rs18234115/s1. The Supplementary Materials comprise a minimal reproducibility dataset containing processed geospatial and tabular data, including NbS candidate geometries and suitability scores, selected intervention portfolios, hydrodynamic simulation outputs, spatial evaluation masks, building-level flood exposure data, water balance diagnostics, and sensitivity analysis results. A README file describing the dataset structure, file specifications, and correspondence with the manuscript, together with a Python verification script (verify_results.py), is also provided to facilitate the independent verification and reproduction of the key quantitative results.

Author Contributions: Conceptualisation, A.-I.G.; methodology, A.-I.G.; software, A.-I.G.; validation, A.-I.G.; formal analysis, A.-I.G., O.A.; investigation, A.-I.G.; resources, A.-I.G.; data curation, A.-I.G., O.A.; writing—original draft preparation, A.-I.G.; writing—review and editing, A.-I.G., A.C. and I.Z.; visualisation, A.-I.G.; supervision, A.C. and I.Z. All authors have read and agreed to the published version of the manuscript.

Funding: This research received no external funding.

Data Availability Statement: The minimal dataset supporting the findings of this study (candidate interventions and scores, selected portfolios, maximum-depth fields of all simulations, evaluation masks, building-level depths and a verification script) is provided as Supplementary Materials.

Acknowledgments: During the preparation of this manuscript, the authors used ChatGPT (OpenAI, GPT-6) and Claude (Anthropic, Opus 5.5) solely for the purpose of language refinement. The authors have reviewed and edited the output and take full responsibility for the content of this publication.

Conflicts of Interest: The authors declare no conflicts of interest.

References

1. Ruangpan, L.; Vojinovic, Z.; Di Sabatino, S.; Leo, L.S.; Capobianco, V.; Oen, A.M.P.; McClain, M.E.; Lopez-Gunn, E. Nature-Based Solutions for Hydro-Meteorological Risk Reduction: A State-of-the-Art Review of the Research Area. *Nat. Hazards Earth Syst. Sci.* **2020**, *20*, 243–270. [CrossRef]
2. Zhou, K.; Kong, F.; Yin, H.; Destouni, G.; Meadows, M.E.; Andersson, E.; Chen, L.; Chen, B.; Li, Z.; Su, J. Urban Flood Risk Management Needs Nature-Based Solutions: A Coupled Social-Ecological System Perspective. *npj Urban Sustain.* **2024**, *4*, 25. [CrossRef]
3. Kuller, M.; Bach, P.M.; Roberts, S.; Browne, D.; Deletic, A. A Planning-Support Tool for Spatial Suitability Assessment of Green Urban Stormwater Infrastructure. *Sci. Total Environ.* **2019**, *686*, 856–868. [CrossRef] [PubMed]
4. Asare, P.; Atun, F.; Pfeffer, K. Spatial Multi-Criteria Analysis for Discovering Nature-Based Solutions Location for Urban Flood Mitigation in Accra. *Appl. Spat. Anal. Policy* **2024**, *17*, 207–239. [CrossRef]
5. Vercruysse, K.; Dawson, D.A.; Glenis, V.; Bertsch, R.; Wright, N.; Kilsby, C. Developing Spatial Prioritization Criteria for Integrated Urban Flood Management Based on a Source-to-Impact Flood Analysis. *J. Hydrol.* **2019**, *578*, 124038. [CrossRef]
6. Dawson, D.A.; Vercruysse, K.; Wright, N. A Spatial Framework to Explore Needs and Opportunities for Interoperable Urban Flood Management. *Philos. Trans. R. Soc. A Math. Phys. Eng. Sci.* **2020**, *378*, 20190205. [CrossRef] [PubMed]
7. Iliadis, C.; Glenis, V.; Kilsby, C. A Cost-Benefit 'Source-Receptor' Framework for Implementation of Blue-Green Flood Risk Management. *J. Hydrol.* **2024**, *634*, 131113. [CrossRef]
8. Parretta, C.; Cortinovis, C.; Formetta, G.; Geneletti, D. Prioritising Nature-Based Solutions for Urban Flood Mitigation in Public and Private Spaces: A Study in Trento, Italy. *Sustain. Cities Soc.* **2026**, *150*, 107904. [CrossRef]
9. Reinstaller, S.; König, A.W.; Muschalla, D. Using High-Resolution Flood Hazard and Urban Heat Island Maps for High-Priority BGI Placement at the City Scale. *Hydrology* **2025**, *12*, 125. [CrossRef]
10. Ur Rehman, A.; Glenis, V.; Lewis, E.; Kilsby, C. Multi-Objective Optimisation Framework for Blue-Green Infrastructure Placement Using Detailed Flood Model. *J. Hydrol.* **2024**, *638*, 131571. [CrossRef]
11. Azadgar, A.; Gańcza, A.; Asl, S.R.; Salata, S.; Nyka, L. Optimizing Nature-Based Solutions for Urban Flood Risk Mitigation: A Multi-Objective Genetic Algorithm Approach in Gdańsk, Poland. *Sci. Total Environ.* **2025**, *963*, 178303. [CrossRef] [PubMed]

12. Theochari, A.P.; Baltas, E. The Nature-Based Solutions and Climate Change Scenarios toward Flood Risk Management in the Greater Athens Area—Greece. *Nat. Hazards* **2024**, *120*, 4729–4747. [CrossRef]
13. Sedighkia, M.; Prinsley, R.; Croke, B.; Alexandra, J. Hydrological and Hydrodynamic Decision Support Tools for Assessing Nature-Based Flood Solutions: Technical Modelling Recommendations and Challenges. *Environ. Model. Softw.* **2026**, *203*, 107040. [CrossRef]
14. Hlal, M.; Baraka Munyaka, J.C.; Chenal, J.; Azmi, R.; Diop, E.B.; Bounabi, M.; Ebnou Abdem, S.A.; Almouctar, M.A.S.; Adraoui, M. Digital Twin Technology for Urban Flood Risk Management: A Systematic Review of Remote Sensing Applications and Early Warning Systems. *Remote Sens.* **2025**, *17*, 3104. [CrossRef]
15. Pérez-Corredor, L.; Hume, S.E.; Alivio, M.B.; Bezak, N. Exploring the Impact of Nature-Based Solutions for Hydrological Extremes Mitigation in Small Mixed Urban-Forest Catchment. *Appl. Sci.* **2024**, *14*, 11813. [CrossRef]
16. Ganos, A.I.; Chassiakos, A.; Zacharias, I. Bridging Urban and Catchment Scales in Urban Pluvial Flooding: A Multi-Resolution Simulation Tool. *Environ. Earth Sci.* **2026**, *85*, 114. [CrossRef]
17. Varlas, G.; Anagnostou, M.N.; Spyrou, C.; Papadopoulos, A.; Kalogiros, J.; Mentzafou, A.; Michaelides, S.; Baltas, E.; Karymbalis, E.; Katsafados, P. A Multi-Platform Hydrometeorological Analysis of the Flash Flood Event of 15 November 2017 in Attica, Greece. *Remote Sens.* **2019**, *11*, 45. [CrossRef]
18. Bellos, V.; Papageorgaki, I.; Kourtis, I.; Vangelis, H.; Kalogiros, I.; Tsakiris, G. Reconstruction of a Flash Flood Event Using a 2D Hydrodynamic Model under Spatial and Temporal Variability of Storm. *Nat. Hazards* **2020**, *101*, 711–726. [CrossRef]
19. Hellenic Survey of Geology and Mineral Exploration (HSGME/EAGME) EAGME Geoportal: Geospatial Data and Maps. Available online: https://www.eagme.gr/site/services?language=en (accessed on 10 February 2026).
20. Adams, J.M.; Gasparini, N.M.; Hobley, D.E.J.; Tucker, G.E.; Hutton, E.W.H.; Nudurupati, S.S.; Istanbulluoglu, E. The Landlab v1.0 OverlandFlow Component: A Python Tool for Computing Shallow-Water Flow across Watersheds. *Geosci. Model Dev.* **2017**, *10*, 1645–1663. [CrossRef]
21. Andreadakis, E.; Diakakis, M.; Nikolopoulos, E.; Spyrou, N.I.; Gogou, M.; Deligiannakis, G.; Katsetsiadou, K.-N.; Argyris, G.; Antoniadis, Z.; Melaki, M.; et al. Characteristics and Impacts of the November 2017 Catastrophic Flash Flood in Mandra, Greece. In Proceedings of the European Geosciences Union General Assembly (EGU 2018), Vienna, Austria, 10 April 2018.
22. Hellenic Ministry of Environment and Energy Rainfall Intensity-Duration-Frequency (IDF) Curves—Second Cycle. Available online: https://floods.ypeka.gr/sdkp-lap/omvries-2round/ (accessed on 21 October 2026).
23. Koutsoyiannis, D.; Xanthopoulos, T. *Engineering Hydrology*, 3rd ed.; National Technical University of Athens: Athens, Greece, 1999; 418p. (In Greek) [CrossRef]
24. De Almeida, G.A.M.; Bates, P.; Freer, J.E.; Souvignet, M. Improving the Stability of a Simple Formulation of the Shallow Water Equations for 2-D Flood Modeling. *Water Resour. Res.* **2012**, *48*, W05528. [CrossRef]
25. Bates, P.D.; Horritt, M.S.; Fewtrell, T.J. A Simple Inertial Formulation of the Shallow Water Equations for Efficient Two-Dimensional Flood Inundation Modelling. *J. Hydrol.* **2010**, *387*, 33–45. [CrossRef]
26. Mein, R.G.; Larson, C.L. Modeling Infiltration during a Steady Rain. *Water Resour. Res.* **1973**, *9*, 384–394. [CrossRef]
27. Arcement, G.J.; Schneider, V.R. *Guide for Selecting Manning's Roughness Coefficients for Natural Channels and Flood Plains*; U.S. Geological Survey Water-Supply Paper 2339; U.S. Government Printing Office: Washington, DC, USA, 1989; 38p. [CrossRef]
28. U.S. Army Corps of Engineers, H.E. Center. HEC-RAS River Analysis System: Hydraulic Reference Manual (Version 6.6). Available online: https://www.hec.usace.army.mil/software/hec-ras/documentation.aspx (accessed on 17 October 2026).
29. Geyik, M.P. *FAO Watershed Management Field Manual: Gully Control*; FAO Conservation Guide 13/2; Food and Agriculture Organization of the United Nations: Rome, Italy, 1986; ISBN 92-5-102482-0.
30. Ontario Ministry of the Environment. *Stormwater Management Planning and Design Manual*; Queen's Printer for Ontario: Toronto, ON, Canada, 2003; ISBN 0-7794-2969-9.
31. Qi, W.; Ma, C.; Xu, H.; Chen, Z.; Zhao, K.; Han, H. Low Impact Development Measures Spatial Arrangement for Urban Flood Mitigation: An Exploratory Optimal Framework Based on Source Tracking. *Water Resour. Manag.* **2021**, *35*, 3755–3770. [CrossRef]

Disclaimer/Publisher's Note: The statements, opinions and data contained in all publications are solely those of the individual author(s) and contributor(s) and not of MDPI and/or the editor(s). MDPI and/or the editor(s) disclaim responsibility for any injury to people or property resulting from any ideas, methods, instructions or products referred to in the content.